

**COLLAPSE ANALYSIS FOR SHELLS
OF GENERAL SHAPE**

VOLUME I ANALYSIS

B. O. ALMROTH

F. A. BROGAN

M. B. MARLOWE

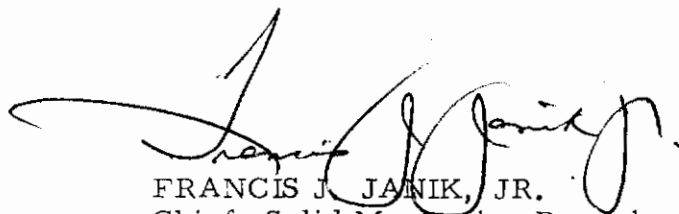
Approved for public release; distribution unlimited.

FOREWORD

This work was prepared by the Lockheed Palo Alto Research Laboratory, Palo Alto, California, under Air Force Contract No. F33615-69-C-1523. It was administered under the Structures Division, Air Force Flight Dynamics Laboratory, with Mr. T. N. Bernstein (FBR) acting as Project Engineer.

This report was completed in January 1972 and covers work performed between April 1969 and January 1972. The supervision of this project was carried out by Mr. B. O. Almroth of the Structural Mechanics Laboratory, LMSC.

This technical report has been reviewed and is approved.



FRANCIS J. JANIK, JR.
Chief, Solid Mechanics Branch
Air Force Flight Dynamics Laboratory

ABSTRACT

This report presents a theory for nonlinear collapse analysis of shells with general shape. The theory combines energy principals and finite difference methods to obtain a system of nonlinear equations; these are solved by a modified Newton-Raphson technique. For greater economy and flexibility in the analysis a capability is provided for use of variable spacing finite difference grids. Inelastic material behavior, as predicted by the White-Besseling Theory, is incorporated into the analysis. A computer code, STAGS, based on the theory has been written and used to solve a number of sample problems. Results for these problems are presented.

TABLE OF CONTENTS

<u>Section</u>		<u>Page</u>
1.0	INTRODUCTION	1
2.0	STAGS THEORY	4
2.1	Metric of the Shell Middle Surface	4
2.2	Curvature Tensor of the Shell Middle Surface	9
2.3	Displacements and Derivatives	12
2.4	Deformation	15
2.5	Strain Energy	17
2.6	Solution Procedure	22
2.7	Bifurcation Buckling	24
2.8	Computation of the Components of the Metric and Curvature Tensors	27
2.9	Physical Components of Strain and Curvature-Change	30
3.0	FINITE DIFFERENCE GRID WITH VARIABLE SPACING	33
4.0	INELASTIC BEHAVIOR	40
4.1	Introduction	40
4.2	The White-Besseling Theory	41
4.3	Implementation of the White-Besseling Theory in STAGS	41
5.0	RESULTS OF SAMPLE CASES	46
5.1	Cylinder with Rectangular Cutout	46
5.2	The Pinched Cylinder	48
5.3	Cylinders with a Circular Cutout	51
5.4	Shells with Elliptic Cross-Section	51
5.5	A Pear-Shaped Cylinder	65
5.6	Bending of Cylindrical Panels Under Point Loading	67
5.7	Inelastic Buckling of Plate	71
6.0	CONCLUSIONS AND RECOMMENDATIONS	77
7.0	REFERENCES	79

LIST OF ILLUSTRATIONS

<u>Figure</u>		<u>Page</u>
1	Coordinate System Used to Define the Shell	5
2	An Elliptic Cone	29
3	Shell Surface Covered with a System of Mesh Lines	34
4	Grid for Cylinder with Circular Cutout	38
5	Stress Strain Curve Showing Bauschinger Effect	42
6	Load-Displacement Curves for a Circular Cylindrical Shell with Cutouts	47
7	Pinched Cylinder	49
8	Lateral Displacements for Pinched Cylinder	49
9	Lateral Displacements for Pinched Cylinder	49
10	Finite Difference Grids	50
11	Finite Difference Grid for Cylinder with Cutout	52
12	Collapse Modes for Cylinder with Circular Cutout	52
13	Load-Displacement Curves for Cylinder with Circular Cutouts	53
14	Load-Displacement Curves for Elliptic Cylinders	55
15	Normal Displacement Versus Axial Load	56
16	Normal Displacement Patterns at the Limit Points	58
17 (a)	Buckling Patterns at Limit Points	59
17 (b)	Buckling Patterns at Limit Points	60
17 (c)	Buckling Patterns at Limit Points	
18	Elliptic Cone	62
19	Ellipse Ratio	63

LIST OF ILLUSTRATIONS (Contd)

<u>Figure</u>		<u>Page</u>
20	Buckling Patterns for Elliptic Cones	64
21	"Pear-Shaped" Cylinder Under Uniform End Shortening - Cylinder Geometry	66
22	"Pear-Shaped" Cylinder Under Uniform End Shortening - Load-Deflection Curves	66
23	"Pear-Shaped" Cylinder Under Uniform End Shortening - Normal Displacement at Midlength at Collapse	66
24	"Pear-Shaped" Cylinder Under Uniform End Shortening - Axial Line Load at Midlength at Collapse	66
25	Cylindrical Panel with Point Load	68
26	Load-Deflection Curves for Cylindrical Panels Loaded Towards the Center	69
27	Load-Displacement Curve for Cylindrical Panel Loaded Away from Center	70
28	Determinant Versus Load Factor	72
29	Plate in Compression	72
30	Load-Displacement Curves for Elastic Plate	73
31	Stress-Strain Curve	75
32	Load-Displacement Curves for Plate with $t = 0.11$ cm	76

Section 1.0 INTRODUCTION

Recent improvements in computer technology and numerical analysis methods have led to significant advances in structural analysis capability. Computer programs are now available for analysis of the static behavior (linear or nonlinear) of almost any shell of revolution subjected to axisymmetric loading. For nonsymmetrical loading or for shells of general shape, a static analysis is readily performed provided that the response is linear. This capability is substantiated in Reference 1. However, nonlinear effects are frequently important in shells. Because these structures are thin, collapse or loss of stability is generally the critical mode of failure. Thicker shells are often subjected to loads of such magnitude that material nonlinearities become important. Reliable and dependable computational systems for this important class of problems have not been developed, although there are computer codes available for some special cases.

Several years ago, a research program was initiated at Lockheed with the goal of developing a computational system for such nonlinear problems. This program has resulted in the STAGS (STRUCTURAL ANALYSIS OF GENERAL SHELLS) computer code for analysis of the static nonlinear response of general shells. STAGS is based on a theory in which the shell surface is subdivided, by means of a finite difference grid work, into a set of subareas. The strain energy density for each subarea is then expressed in terms of displacement components and their derivatives. After the derivatives have been replaced by their finite difference equivalents, the energy can be calculated and, together with the potential energy due to applied loads, summed over the shell surface. The total potential energy expression of the shell so obtained is then minimized according to familiar energy principles and a system of nonlinear algebraic equations

in the unknown displacements results. These equations are solved by a Newton-Raphson technique.

STAGS is an outgrowth of work on the buckling of cylindrical panels with nonuniform membrane stresses that was initiated at LMSC in 1963 under the sponsorship of NASA Marshall Space Flight Center (Ref. 2). The basic nonlinear computer program for cylindrical shells with cutouts (Ref. 3) and a linear version including analysis of free vibrations (Ref. 4) were developed under the LMSC Independent Research Program. Under contract with the Naval Ship Research and Development Center (NSRDC), the linear version of the code was developed to include shells of revolution with smooth but otherwise arbitrary cutouts (Ref. 5).

The work reported here extends the nonlinear version to shells of more general shapes with cutouts of arbitrary contour. In addition, inelastic deformations and a capability to handle a finite difference grid with variable nodal point spacing have been added. In a parallel effort funded by Lockheed's Independent Research Program, the equations were further generalized to include nonorthogonal coordinates (Ref. 6). As this work was completed before the end of the contract period, it was possible to include the more general equations in this report.

Further expansion of the STAGS program has been accomplished under parallel research studies funded by the Air Force Space and Missile Systems Organization (SAMSO) and by the NASA Langley Research Center. During the now completed SAMSO study, provisions were made in the STAGS code to allow both the temperature and material properties to vary over the surface and through the thickness of the shell. In addition, a bifurcation buckling branch was added. Parameter studies were made to evaluate the applicability of the bifurcation buckling approach to reentry vehicle analysis (Ref. 7). Although most of these extensions were made primarily to render STAGS suitable for reentry vehicle analysis, they have considerably enhanced the overall capability of the code.

The NASA study is currently in progress. Under this study, STAGS is being developed to handle segmented and branched shells, and to treat

Contrails

realistic types of shell wall constructions including those which involve anisotropic materials. Finite difference expressions based on non-rectangular grids and an automatic grid generator are also being added. A time integration scheme will be developed and included in STAGS. This will permit the solution of dynamic response and dynamic buckling problems. The NASA work is scheduled for completion by the summer of 1972.

A STAGS user's manual that documents all of the modifications completed to date has been prepared (Ref. 8).

Section 2.0 STAGS THEORY

In the application of finite difference techniques to shell analysis, it has been customary to assume that lines of curvature constitute the surface coordinate lines which form the finite difference mesh. This assumption results in orthogonal coordinate lines and leads to simple shell equations; however, there is a serious disadvantage to this approach in that in many instances shell boundaries do not lie along lines of curvature. When this occurs, boundary conditions can be approximated at best, and then only with the introduction of extreme mathematical complexities. For this reason, it is advantageous to formulate the shell theory in terms of generalized coordinates so that boundaries coincide with particular coordinate lines.

This section presents the generalized theory upon which the STAGS computer code is based. Although no attempt is made to be exhaustive in the coverage of the basic shell theory, a brief description of the fundamental aspects is given. For additional material, the reader is referred to Reference 9. In addition, methods for computing the shell middle surface input parameters are presented.

2.1 Metric of the Shell Middle Surface

Consider a surface in space, described by coordinates φ^1 and φ^2 , which is embedded in a three dimensional Euclidean space defined by the Cartesian coordinates, x^1 , x^2 , and x^3 , as shown in Figure 1. The vector \bar{r} to any point on the surface can be written as

$$\begin{aligned}\bar{r} &= x^1 \bar{k}_1 + x^2 \bar{k}_2 + x^3 \bar{k}_3 \\ &= x^i \bar{k}_i\end{aligned}\tag{1}$$

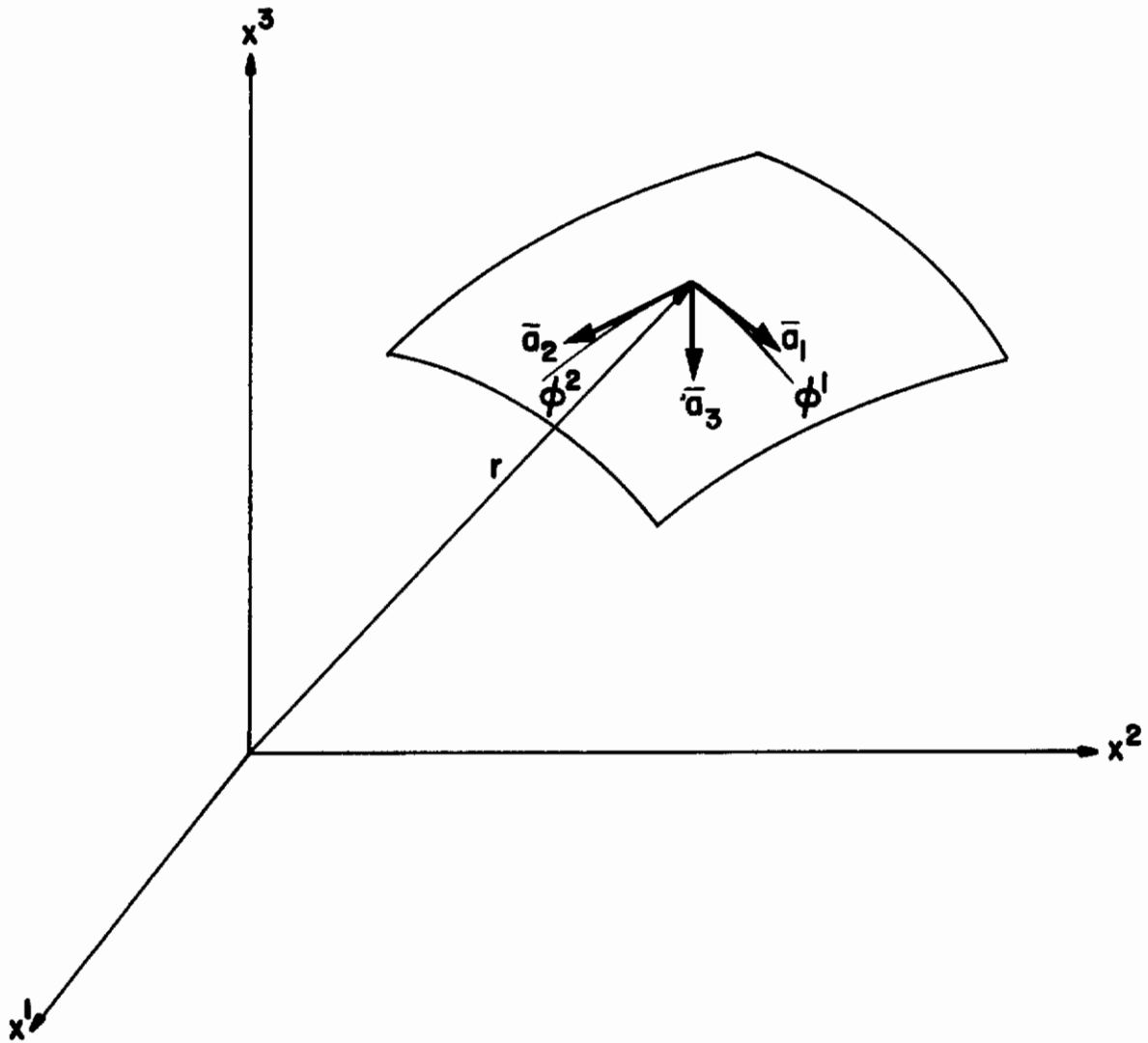


Figure 1 Coordinate System Used to Define the Shell

Contrails

where the \bar{k}_i are unit vectors in the x^i directions, respectively. Now consider the differential

$$\begin{aligned}d\bar{r} &= dx^1 \bar{k}_1 + dx^2 \bar{k}_2 + dx^3 \bar{k}_3 \\ &= dx^i \bar{k}_i\end{aligned}\tag{2}$$

and define this expression for $d\bar{r}$ in terms of the shell coordinates φ^1 and φ^2 by

$$\begin{aligned}d\bar{r} &\equiv \bar{a}_1 d\varphi^1 + \bar{a}_2 d\varphi^2 \\ &= \bar{a}_\alpha d\varphi^\alpha\end{aligned}\tag{3}$$

The quantities \bar{a}_1, \bar{a}_2 are called the covariant base vectors and can be written as

$$\begin{aligned}\bar{a}_\alpha &= \bar{k}_1 \frac{\partial x^1}{\partial \varphi^\alpha} + \bar{k}_2 \frac{\partial x^2}{\partial \varphi^\alpha} + \bar{k}_3 \frac{\partial x^3}{\partial \varphi^\alpha} \\ &= \bar{k}_i \frac{\partial x^i}{\partial \varphi^\alpha}\end{aligned}\tag{4}$$

It should be noted that, in general, the base vectors \bar{a}_α are not unit vectors but have magnitudes given by

$$\begin{aligned}|\bar{a}_1| &= \sqrt{\bar{a}_1 \cdot \bar{a}_1} \\ |\bar{a}_2| &= \sqrt{\bar{a}_2 \cdot \bar{a}_2}\end{aligned}\tag{5}$$

The expression for incremental arc length on the shell middle surface is

$$ds^2 = d\bar{r} \cdot d\bar{r}$$

or

Contrails

$$\begin{aligned} ds^2 &= a_{11} d\varphi^1 d\varphi^1 + 2 a_{12} d\varphi^1 d\varphi^2 + a_{22} d\varphi^2 d\varphi^2 \\ &= a_{\alpha\beta} d\varphi^\alpha d\varphi^\beta \end{aligned} \tag{6}$$

The quantities $a_{\alpha\beta}$ are called the components of the covariant metric tensor, and are defined by

$$a_{\alpha\beta} = \bar{a}_\alpha \cdot \bar{a}_\beta \tag{7}$$

Two alternate forms of Eq. (6) are

$$\begin{aligned} ds^2 &= A^2 d\varphi^1 d\varphi^1 + 2 C d\varphi^1 d\varphi^2 + B^2 d\varphi^2 d\varphi^2 \\ ds^2 &= A^2 d\varphi^1 d\varphi^1 + 2 A B \cos \theta d\varphi^1 d\varphi^2 + B^2 d\varphi^2 d\varphi^2 \end{aligned}$$

Both of these formulations have been used in the STAGS User's Manuals; the quantities A, B, C, and θ are related to the components of the metric tensor by

$$\begin{aligned} A &= \sqrt{a_{11}} \\ B &= \sqrt{a_{22}} \\ C &= A B \cos \theta = a_{12} \\ \cos \theta &= \frac{a_{12}}{\sqrt{a_{11} a_{22}}} \end{aligned} \tag{8}$$

It can be seen from Eqs. (3, 5, 7, 8) that A and B are measures of the length along the coordinate lines φ^1 and φ^2 , and that θ is the angle between these lines.

Contrails

Since the covariant base vectors \bar{a}_1, \bar{a}_2 are not necessarily normal to one another, it is sometimes convenient to consider a set of vectors defined by

$$\begin{aligned}\bar{a}^1 &\equiv \frac{1}{\sqrt{a}} \bar{a}_2 \times \bar{a}_3 \\ \bar{a}^2 &\equiv \frac{1}{\sqrt{a}} \bar{a}_3 \times \bar{a}_1\end{aligned}\tag{9}$$

where \bar{a}_3 is the unit normal vector as shown in Figure 1 and a is the determinant of the metric tensor

$$\begin{aligned}\bar{a}_3 &\equiv \frac{1}{\sqrt{a}} \bar{a}_1 \times \bar{a}_2 \\ a &\equiv |a_{\alpha\beta}| = a_{11} a_{22} - a_{12}^2\end{aligned}\tag{10}$$

The vectors defined by Eqs. (9) are called contravariant base vectors and have the properties

$$\begin{aligned}\bar{a}^1 \cdot \bar{a}_1 &= 1 \\ \bar{a}^2 \cdot \bar{a}_2 &= 1 \\ \bar{a}^1 \cdot \bar{a}_2 &= 0 \\ \bar{a}^2 \cdot \bar{a}_1 &= 0\end{aligned}\tag{11}$$

or

$$\bar{a}_\alpha \cdot \bar{a}^\beta = \delta_\alpha^\beta\tag{12}$$

δ_α^β is the Kronecker delta and has the properties

$$\delta_{\alpha}^{\beta} = \begin{cases} 1, & \alpha = \beta \\ 0, & \alpha \neq \beta \end{cases} \quad (13)$$

The contravariant metric tensor components are defined by

$$a^{\alpha\beta} \equiv \bar{a}^{\alpha} \cdot \bar{a}^{\beta} \quad (14)$$

which can be written in terms of a_{α} as

$$\begin{aligned} a^{11} &= \frac{a_{22}}{a} \\ a^{22} &= \frac{a_{11}}{a} \\ a^{12} &= \frac{a_{12}}{a} \end{aligned} \quad (15)$$

With the aid of Eqs. (10 through 15), Eqs. (9) can be written in the form

$$\bar{a}^{\alpha} = a^{\alpha\beta} \bar{a}_{\beta} \quad (16)$$

2.2 Curvature Tensor of the Shell Middle Surface

The curvature and twist of a surface are defined by the curvature and torsion of lines embedded in the surface relative to the unit normal vector. For instance, the normal curvatures of a surface with respect to the coordinate lines φ^1 and φ^2 are defined by

$$\begin{aligned} b_{n1} &\equiv \bar{b}_1 \cdot \bar{a}_3 \\ b_{n2} &\equiv \bar{b}_2 \cdot \bar{a}_3 \end{aligned}$$

where \bar{b}_1 and \bar{b}_2 are the curvature vectors of the coordinate lines φ^1

Contraills

and φ^2 , respectively. These vectors can be written as

$$\bar{b}_1 = \frac{d}{ds_1} \left(\frac{\bar{a}_1}{\sqrt{a_{11}}} \right)$$

$$\bar{b}_2 = \frac{d}{ds_2} \left(\frac{\bar{a}_2}{\sqrt{a_{22}}} \right)$$

where ds_1 and ds_2 are given by

$$ds_1 = \sqrt{a_{11}} d\varphi^1$$

$$ds_2 = \sqrt{a_{22}} d\varphi^2$$

Hence, the normal curvatures of the shell middle surface are

$$b_{n1} = \frac{1}{\sqrt{a_{11}}} \frac{d}{d\varphi^1} \left(\frac{\bar{a}_1}{\sqrt{a_{11}}} \right) \cdot \bar{a}_3 \tag{17}$$

$$b_{n2} = \frac{1}{\sqrt{a_{22}}} \frac{d}{d\varphi^2} \left(\frac{\bar{a}_2}{\sqrt{a_{22}}} \right) \cdot \bar{a}_3$$

The twist of a surface with respect to a coordinate line is the torsion of the coordinate line with the sign chosen such that a positive twist occurs when the normal vector \bar{a}_3 rotates about one coordinate line towards the other coordinate line. This leads to the definitions for twist of a surface

$$b_{t1} \equiv - \frac{1}{\sqrt{a_{11}}} \frac{d\bar{a}_3}{d\varphi^1} \cdot \frac{\bar{a}_2}{\sqrt{a_{22}}} \tag{18}$$

$$b_{t2} \equiv - \frac{1}{\sqrt{a_{22}}} \frac{d\bar{a}_3}{d\varphi^2} \cdot \frac{\bar{a}_1}{\sqrt{a_{11}}}$$

The curvature tensor of a surface is defined by

$$b_{\alpha\beta} \equiv - \frac{\partial \bar{a}_3}{\partial \phi^\alpha} \cdot \bar{a}_\beta \quad (19)$$

This is a symmetric tensor whose indices are raised and lowered according to

$$\begin{aligned} b_\alpha^\beta &= b_{\alpha\rho} a^{\rho\beta} = b^{\beta\rho} a_{\rho\alpha} \\ b_{\alpha\beta} &= b_\alpha^\rho a_{\rho\beta} \\ b^{\alpha\beta} &= b_\rho^\alpha a^{\rho\beta} \end{aligned} \quad (20)$$

The components of $b_{\alpha\beta}$ are related to the changes in normal curvature and twist by

$$\begin{aligned} b_{n\alpha} &= \frac{b_{\alpha\alpha}}{\sqrt{a_{\alpha\alpha}}} \quad (\alpha \text{ not summed}) \\ b_{t\alpha} &= \frac{b_\alpha^\beta}{\sqrt{a_{\alpha\alpha} a_{\beta\beta}}} \quad (\alpha \neq \beta; \alpha, \beta \text{ not summed}) \end{aligned} \quad (21)$$

It can be seen with the aid of Eqs. (10, 15, 20) that, for orthogonal coordinates ($a_{12} = 0$), $b_{t1} = b_{t2}$.

Two invariants associated with the curvature are the mean curvature H and the Gaussian curvature K

$$\begin{aligned} H &\equiv \frac{1}{2} b_\alpha^\alpha \\ K &\equiv \frac{1}{2} \left(b_\alpha^\alpha b_\beta^\beta - b_\beta^\alpha b_\alpha^\beta \right) \end{aligned} \quad (22)$$

2.3 Displacements and Derivatives

The displacement vector of a point on the shell middle surface is defined by

$$\bar{u} = u^\alpha \bar{a}_\alpha + w \bar{a}_3 \quad (23a)$$

The quantities u^α are called the contravariant components of in-plane displacement. An alternate form of (23a) is

$$\bar{u} = u_\alpha \bar{a}^\alpha + w \bar{a}_3 \quad , \quad (23b)$$

where the u_α are the covariant components of in-plane displacement. Since \bar{a}_3 is a unit vector and normal to \bar{a}_α and \bar{a}^α , there is no distinction between covariance and contravariance for w . From Eq. (16) it can be seen that u^α and u_α are related by

$$\begin{aligned} u^\alpha &= a^{\alpha\beta} u_\beta \\ u_\alpha &= a_{\alpha\beta} u^\beta \end{aligned} \quad (24)$$

The covariant and contravariant displacement components can be related to physical quantities. Consider the displacement vector written in terms of unit covariant vectors

$$\bar{u} = u \frac{\bar{a}_1}{\sqrt{a_{11}}} + v \frac{\bar{a}_2}{\sqrt{a_{22}}} + w \bar{a}_3 \quad (25)$$

The quantities u and v represent the physical components of in-plane displacement in the directions defined by the covariant base vectors a_1 and a_2 , respectively. Equating Eqs. (22, 23) to Eq. (25) with help from Eqs. (7, 14, 16) yields

Contrails

$$u_1 = \sqrt{a_{11}} u + \frac{a_{12}}{\sqrt{a_{22}}} v \quad (26)$$

$$u_2 = \frac{a_{12}}{\sqrt{a_{11}}} u + \sqrt{a_{22}} v$$

and

$$u^1 = \frac{u}{\sqrt{a_{11}}} \quad (27)$$

$$u^2 = \frac{v}{\sqrt{a_{22}}}$$

The partial derivative of the covariant base vectors are defined by

$$\frac{\partial \bar{a}_\alpha}{\partial \varphi^\beta} \equiv \Gamma_{\beta\alpha}^\rho \bar{a}_\rho + b_{\alpha\beta} \bar{a}_3 \quad (28)$$

The $b_{\alpha\beta} \bar{a}_3$ term can be deduced from Eq. (19). It follows from Eq. (16) that $\Gamma_{\alpha\beta}^\rho$ can be written as

$$\Gamma_{\alpha\beta}^\rho = \Gamma_{\beta\alpha}^\rho = \frac{\partial \bar{a}_\alpha}{\partial \varphi^\beta} \cdot \bar{a}^\rho \quad (29)$$

The partial derivatives of the contravariant base vectors can be deduced from Eq. (28, 29) as

$$\frac{\partial \bar{a}^\alpha}{\partial \varphi^\beta} = - \Gamma_{\beta\rho}^\alpha \bar{a}^\rho + b_\beta^\alpha \bar{a}_3 \quad (30)$$

The quantities $\Gamma_{\alpha\beta}^\rho$ are Christoffel symbols of the second kind. Symbols

of the first kind are defined by lowering the upper index

$$\Gamma_{\alpha\beta\rho} = \Gamma_{\alpha\beta}^{\lambda} a_{\lambda\rho} = \frac{\partial \bar{a}_{\alpha}}{\partial \varphi^{\beta}} \cdot \bar{a}_{\rho} \quad (31)$$

These quantities expressed in terms of the partial derivatives of $a_{\alpha\beta}$ are

$$\Gamma_{\alpha\beta\rho} = \frac{1}{2} \left(\frac{\partial a_{\alpha\rho}}{\partial \varphi^{\beta}} + \frac{\partial a_{\beta\rho}}{\partial \varphi^{\alpha}} - \frac{\partial a_{\alpha\beta}}{\partial \varphi^{\rho}} \right) \quad (32)$$

With the aid of Eqs. (28, 30), the partial derivative of the displacement vector u [Eq. (22, 23)] can be written as

$$\begin{aligned} \frac{\partial \bar{u}}{\partial \varphi^{\alpha}} &= u^{\beta} |_{\alpha} \bar{a}_{\beta} + b_{\alpha}^{\beta} u_{\beta} \bar{a}_3 - b_{\alpha}^{\beta} w \bar{a}_{\beta} + \frac{\partial w}{\partial \varphi^{\alpha}} \bar{a}_3 \\ &= u_{\beta} |_{\alpha} \bar{a}^{\beta} + b_{\alpha}^{\beta} u_{\beta} \bar{a}_3 - b_{\alpha}^{\beta} w \bar{a}_{\beta} + \frac{\partial w}{\partial \varphi^{\alpha}} \bar{a}_3 \end{aligned} \quad (33)$$

The quantities $u_{\beta} |_{\alpha}$ and $u^{\beta} |_{\alpha}$ are called the covariant derivatives of u_{β} and u^{β} with respect to φ^{α} and are given by

$$\begin{aligned} u_{\beta} |_{\alpha} &= \frac{\partial u_{\beta}}{\partial \varphi^{\alpha}} - \Gamma_{\beta\alpha}^{\rho} u_{\rho} \\ u^{\beta} |_{\alpha} &\equiv \frac{\partial u^{\beta}}{\partial \varphi^{\alpha}} + \Gamma_{\rho\alpha}^{\beta} u^{\rho} \end{aligned} \quad (34)$$

The concept of covariant differentiation can be extended to second order tensors such as $b_{\alpha\beta}$.

$$b_{\alpha\beta}|_{\rho} \equiv \frac{\partial b_{\alpha\beta}}{\partial \varphi^{\rho}} - \Gamma_{\alpha\rho}^{\lambda} b_{\beta\lambda} - \Gamma_{\beta\rho}^{\lambda} b_{\alpha\lambda} \quad (35)$$

$$b_{\alpha}^{\beta}|_{\rho} \equiv \frac{\partial b_{\alpha}^{\beta}}{\partial \varphi^{\rho}} + \Gamma_{\rho\lambda}^{\beta} b_{\alpha}^{\lambda} - \Gamma_{\rho\alpha}^{\lambda} b_{\lambda}^{\beta} .$$

The quantities appearing in Eqs. (33) can be regrouped to define the displacement gradients $\gamma_{\alpha\beta}$ and β_{α}

$$\gamma_{\alpha\beta} \equiv u_{\alpha}|_{\beta} - b_{\alpha\beta} w \quad (36)$$

$$\beta_{\alpha} \equiv \frac{\partial w}{\partial \varphi^{\alpha}} + b_{\alpha}^{\beta} u_{\beta} .$$

Hence, the derivatives of \bar{u} take the form

$$\frac{\partial \bar{u}}{\partial \varphi^{\alpha}} = \gamma_{\beta\alpha} \bar{a}^{\beta} + \beta_{\alpha} \bar{a}_3 . \quad (37)$$

2.4 Deformation

The deformation of the shell middle surface can be specified in terms of the changes in the metric and curvature tensors. With the deformed state of the shell characterized by a tilda ($\tilde{a}_{\alpha\beta}$, $\tilde{b}_{\alpha\beta}$), the strain and curvature-change tensors can be defined by

$$\begin{aligned} 2 \epsilon_{\alpha\beta} &\equiv \tilde{a}_{\alpha\beta} - a_{\alpha\beta} \\ \kappa_{\alpha}^{\beta} &\equiv \tilde{b}_{\alpha}^{\beta} - b_{\alpha}^{\beta} \end{aligned} \quad (38)$$

It can be seen with the aid of Eqs. (6, 13, 22) that these definitions lead directly to the changes in incremental arc length and mean curvature

$$\begin{aligned} d\tilde{s}^2 - ds^2 &= 2 \epsilon_{\alpha\beta} d\varphi^\alpha d\varphi^\beta \\ \tilde{H} - H &= \frac{1}{2} \kappa_{\alpha}^{\cdot\beta} \delta_{\beta}^{\alpha} \end{aligned} \quad (39)$$

Although $\epsilon_{\alpha\beta}$ and $\kappa_{\alpha}^{\cdot\beta}$ are independent of any particular metric tensor, it is convenient to refer these quantities to the metric of the undeformed middle surface; i. e., in operations expressing, for instance, covariant strain or curvature-change tensors in terms of contravariant tensors (or vice versa) $a^{\alpha\beta}$ and $a_{\alpha\beta}$ are used rather than $\tilde{a}^{\alpha\beta}$ and $\tilde{a}_{\alpha\beta}$. For example,

$$\begin{aligned} \epsilon_{\alpha}^{\beta} &= \epsilon_{\alpha\rho} a^{\rho\beta} \\ \kappa_{\alpha\beta} &= \kappa_{\alpha}^{\cdot\rho} a_{\rho\beta} \end{aligned} \quad * \quad (40)$$

In addition to strain and curvature-change, portions of the shell middle surface may undergo finite rotations. If such is the case, the expressions for $\epsilon_{\alpha\beta}$ and $\kappa_{\alpha\beta}$, when written in terms of the displacement gradients, must reflect this. Since the general expressions for $\epsilon_{\alpha\beta}$ and $\kappa_{\alpha\beta}$ are extremely complicated, it is desirable to use simpler, approximate expressions whenever possible.

The rotation of any part of the shell middle surface can be split

* $\kappa_{\alpha\beta}$ is not generally symmetric; therefore, its indices must be moved straight up and down only. The dot appearing over the α assures this. Note that a dot in the terms $\epsilon_{\alpha}^{\cdot\beta}$, $\epsilon_{\cdot\alpha}^{\beta}$ is not required since $\epsilon_{\alpha\beta} = \epsilon_{\beta\alpha}$; hence, for symmetric tensors, no distinction in the ordering of indices is required.

into two parts, an out-of-plane rotation or "tilt" and an in-plane rotation commonly called the "rotation about the normal." When the angle of tilt (Ω) is moderate, the tilt and in-plane rotation (ω) can be approximated by

$$\sin \omega \approx \frac{1}{2\sqrt{a}} (\gamma_{21} - \gamma_{12}) \quad (41)$$

$$\sin^2 \Omega \approx \beta^\alpha \beta_\alpha \quad .$$

The expressions for $\epsilon_{\alpha\beta}$ and $\kappa_{\alpha\beta}$ used in STAGS are

$$\epsilon_{\alpha\beta} = \frac{1}{2} (\gamma_{\alpha\beta} + \gamma_{\beta\alpha}) + \frac{1}{2} \gamma_{\rho\alpha} \gamma_{\cdot\beta}^\rho + \frac{1}{2} \beta_\alpha \beta_\beta \quad (42)$$

$$\kappa_{\alpha\beta} = \beta_\beta |_\alpha + b_\alpha^\rho \gamma_{\rho\beta} - b_{\alpha\beta} \gamma_{\cdot\rho}^\rho \quad .$$

These approximations are based upon the assumptions that the tilt can be moderately large ($\Omega < .3$) and that the in-plane rotation is of the same order of magnitude as the square root of a typical middle surface strain ($\omega = 0 (\sqrt{\epsilon})$). A complete derivation of the above is given in Reference 9. Physical components of strain and curvature-change for lines of curvature coordinates are given in Section 2.9.

2.5 Strain Energy

The strain energy density for thin elastic shells is

$$U = \frac{1}{2} \frac{E}{1-\nu^2} \left[(1-\nu) a^{\alpha\rho} a^{\beta\lambda} + \nu a^{\alpha\beta} a^{\rho\lambda} \right] \left[t \epsilon_{\alpha\beta} \epsilon_{\rho\lambda} + \frac{t^3}{12} \kappa_{\alpha\beta} \kappa_{\rho\lambda} \right] \quad (43)$$

For shell coordinates ξ and η and with the use of Eqs. (8, 15), Eq. (43)

Contraills

can be cast in the form

$$\begin{aligned}
 U = & \frac{D}{2} \left\{ (A \sin \theta)^{-4} \epsilon_{\xi\xi}^2 - \frac{4A \cos \theta}{B} (A \sin \theta)^{-4} \epsilon_{\xi\xi} \epsilon_{\xi\eta} \right. \\
 & + 2 [1-(1-\nu) \sin^2 \theta] (AB \sin^2 \theta)^{-2} \epsilon_{\xi\xi} \epsilon_{\eta\eta} + 2 (AB \sin^2 \theta)^{-2} [(1-\nu) + (1+\nu) \cos^2 \theta] \epsilon_{\xi\eta}^2 \\
 & \left. - \frac{4B \cos \theta}{A} (B \sin \theta)^{-4} \epsilon_{\xi\eta} \epsilon_{\eta\eta} + (B \sin \theta)^{-4} \epsilon_{\eta\eta}^2 \right\} \\
 & + \frac{K}{2} \left\{ (A \sin \theta)^{-4} \kappa_{\xi\xi}^2 - \frac{4A \cos \theta}{B} (A \sin \theta)^{-4} \kappa_{\xi\xi} \kappa_{\xi\eta} \right. \\
 & + 2 [1-(1-\nu) \sin^2 \theta]^{-2} (AB \sin^2 \theta)^{-2} \kappa_{\xi\xi} \kappa_{\eta\eta} + 2 (AB \sin^2 \theta)^{-2} [(1-\nu) \cos^2 \theta] \kappa_{\xi\eta}^2 \\
 & \left. - \frac{4B \cos \theta}{A} (B \sin \theta)^{-4} \kappa_{\eta\eta} \kappa_{\xi\eta} + (B \sin \theta)^{-4} \kappa_{\eta\eta}^2 \right\}
 \end{aligned} \tag{44}$$

where D and K are the membrane and bending stiffnesses, respectively.

$$\begin{aligned}
 D & \equiv \frac{Et}{1-\nu^2} \\
 K & \equiv \frac{Et^3}{12(1-\nu^2)}
 \end{aligned} \tag{45}$$

The covariant components of strain and curvature-change expressed in terms of the displacement gradients are

Contrails

$$\begin{aligned}
 e_{\xi\xi} &= \gamma_{\xi\xi} + \frac{1}{2} \left(\gamma_{\xi\xi} \gamma_{\cdot\xi}^{\xi} + \gamma_{\eta\xi} \gamma_{\cdot\xi}^{\eta} + \beta_{\xi} \beta_{\xi} \right) \\
 e_{\xi\eta} &= \frac{1}{2} \left(\gamma_{\xi\eta} + \gamma_{\eta\xi} + \gamma_{\xi\xi} \gamma_{\cdot\xi}^{\eta} + \gamma_{\eta\xi} \gamma_{\cdot\eta}^{\xi} + \beta_{\xi} \beta_{\eta} \right) \\
 e_{\eta\eta} &= \gamma_{\eta\eta} + \frac{1}{2} \left(\gamma_{\xi\eta} \gamma_{\cdot\eta}^{\xi} + \gamma_{\eta\eta} \gamma_{\cdot\eta}^{\eta} + \beta_{\eta} \beta_{\eta} \right)
 \end{aligned} \tag{46}$$

$$\begin{aligned}
 \kappa_{\xi\xi} &= \beta_{\xi,\xi} - \Gamma_{\xi\xi}^{\xi} \beta_{\xi} - \Gamma_{\xi\xi}^{\eta} \beta_{\eta} + b_{\xi\eta} \gamma_{\cdot\xi}^{\eta} - b_{\xi\xi} \gamma_{\cdot\eta}^{\xi} \\
 \kappa_{\xi\eta} &= \frac{1}{2} \left[\beta_{\xi,\eta} + \beta_{\eta,\xi} - \Gamma_{\xi\eta}^{\xi} \beta_{\xi} - \Gamma_{\xi\eta}^{\eta} \beta_{\eta} + b_{\xi\xi} \gamma_{\cdot\xi}^{\eta} + b_{\eta\eta} \gamma_{\cdot\eta}^{\xi} \right. \\
 &\quad \left. - b_{\xi\eta} \gamma_{\cdot\xi}^{\xi} - b_{\xi\eta} \gamma_{\cdot\eta}^{\eta} \right] \\
 \kappa_{\eta\eta} &= \beta_{\eta,\eta} - \Gamma_{\eta\eta}^{\xi} \beta_{\xi} - \Gamma_{\eta\eta}^{\eta} \beta_{\eta} + b_{\xi\eta} \gamma_{\cdot\eta}^{\xi} - b_{\eta\eta} \gamma_{\cdot\xi}^{\eta}
 \end{aligned} \tag{47}$$

where the commas denote partial differentiation. The displacement gradients written as functions of the physical components of displacement u and v are (see Eqs. (8, 26, 27, 34, 36))

$$\begin{aligned}
 \beta_{\xi} &= w_{,\xi} + \frac{1}{A} b_{\xi\xi} u + \frac{1}{B} b_{\xi\eta} v \\
 \beta_{\eta} &= w_{,\eta} + \frac{1}{A} b_{\xi\eta} u + \frac{1}{B} b_{\eta\eta} v
 \end{aligned} \tag{48}$$

Contrails

$$\gamma_{\xi\xi} = Au,_{\xi} + A/B (A,_{\xi} - B,_{\xi} \cos \theta) v + A \cos \theta v,_{\xi} - b_{\xi\xi} w$$

$$\gamma_{\xi\eta} = Au,_{\eta} + [(A \cos \theta),_{\eta} - B,_{\xi}] v + A \cos \theta v,_{\eta} - b_{\xi\eta} w$$

$$\gamma_{\eta\xi} = [(B \cos \theta),_{\xi} - A,_{\eta}] u + B \cos \theta u,_{\xi} + B v,_{\xi} - b_{\xi\eta} w$$

$$\gamma_{\eta\eta} = B/A (B,_{\eta} - A,_{\eta} \cos \theta) u + B \cos \theta u,_{\eta} + B v,_{\eta} - b_{\eta\eta} w$$

$$\begin{aligned} \gamma,_{\xi}^{\xi} &= 1/A u,_{\xi} + [(\cos \theta / (AB \sin^2 \theta)) [A,_{\eta} - (B \cos \theta),_{\xi}] u \\ &\quad + [1 / (AB \sin^2 \theta)] [A,_{\eta} - \cos \theta B,_{\xi}] v - b_{\xi\xi}^{\xi} w \end{aligned} \quad (49)$$

$$\begin{aligned} \gamma,_{\eta}^{\xi} &= 1/A u,_{\eta} + [1 / (A^2 \sin^2 \theta)] [(A \cos \theta),_{\eta} - B,_{\xi}] v \\ &\quad + [\cos \theta / (A^2 \sin^2 \theta)] [A,_{\eta} \cos \theta - B,_{\xi}] u - b_{\eta\xi}^{\xi} w \end{aligned}$$

$$\begin{aligned} \gamma,_{\xi}^{\eta} &= 1/B v,_{\xi} + [1 / (B^2 \sin^2 \theta)] [(B \cos \theta),_{\xi} - A,_{\eta}] u \\ &\quad + [\cos \theta / (B^2 \sin^2 \theta)] [B,_{\xi} \cos \theta - A,_{\eta}] v - b_{\xi\eta}^{\eta} w \end{aligned}$$

$$\begin{aligned} \gamma,_{\eta}^{\eta} &= 1/B v,_{\eta} + [\cos \theta / (AB \sin^2 \theta)] [B,_{\xi} - (A \cos \theta),_{\eta}] v \\ &\quad + [1 / (AB \sin^2 \theta)] [B,_{\xi} - \cos \theta A,_{\eta}] u - b_{\eta\eta}^{\eta} w \end{aligned}$$

and the Christoffel symbols are (Eqs. (8, 32))

$$\begin{aligned}
 \Gamma_{\xi\xi}^{\xi} &= [BA,_{\xi} + (AA,_{\eta} - C,_{\xi}) \cos \theta] / (AB \sin^2 \theta) \\
 \Gamma_{\xi\xi}^{\eta} &= [C,_{\xi} - BA,_{\xi} \cos \theta - AA,_{\eta}] / (B^2 \sin^2 \theta) \\
 \Gamma_{\xi\eta}^{\xi} &= [A,_{\eta} - B,_{\xi} \cos \theta] / (A \sin^2 \theta) \\
 \Gamma_{\xi\eta}^{\eta} &= [B,_{\xi} - A,_{\eta} \cos \theta] / (B \sin^2 \theta) \\
 \Gamma_{\eta\eta}^{\xi} &= [C,_{\eta} - BB,_{\xi} - AB,_{\eta} \cos \theta] / (A^2 \sin^2 \theta) \\
 \Gamma_{\eta\eta}^{\eta} &= [AB,_{\eta} + (BB,_{\xi} - C,_{\eta}) \cos \theta] / (AB \sin^2 \theta)
 \end{aligned} \tag{50}$$

Substitution of Eqs. (48-50) into Eqs. (46, 47) yields the covariant strain and curvature-change tensors as functions of the physical displacement components u , v , and w . These equations are then substituted into Eq. (44) to obtain the strain energy as a function of the displacements.

The effects of geometric imperfections have been accounted for by modifying Eqs. (46) to include small values of an initial normal displacement \hat{w} . The terms $\hat{w},_{\xi}^{\beta\xi}$, $\hat{w},_{\eta}^{\beta\eta}$ and $\hat{w},_{\xi}^{\beta\xi} + \hat{w},_{\eta}^{\beta\xi}$ were added to the three middle surface strain $\epsilon_{\xi\xi}$, $\epsilon_{\eta\eta}$, and $\epsilon_{\xi\eta}$, respectively.

Geometric imperfections are important because the critical loads of many shells are sensitive to such imperfections. In addition, there are many cases where there exist planes of symmetry with respect to loading and geometry. In such cases, antimetric deformations will only be found if they are "triggered" by the inclusion of antimetric geometric imperfections.

2.6 Solution Procedure

The solution procedure used in STAGS is based on the principle of stationary potential energy. After the expression for strain energy density is formed, as explained in the previous section, the displacements and their derivatives are replaced by appropriate finite difference expressions. (A set of finite difference expressions for grids with variable spacing is described in Section 3.0.) The strain energy density at mesh station i is then written in the form

$$\Delta U^i = \frac{1}{2} Z^{i*} D^i Z^i \quad (51)$$

where D is a 6×6 matrix of constants and Z^i is the vector of strains and curvature changes at station i . (In this report all vectors are understood to be column vectors and $*$ designates the adjoint operator. Thus, Z^{i*} is a row vector.) The matrix D^i is obtained by integration through the shell wall and is a function of the geometric parameters of the shell and of the material properties. The strain vector Z^i is a nonlinear (quadratic) function of the displacement unknowns and the geometric parameters. The vector of stress resultants at station i is given by

$$S^i = D^i Z^i \quad (52)$$

The total strain energy of the shell is then

$$U = \sum_i \Delta U^i a^i \quad (53)$$

where a^i is the area of the i^{th} mesh subregion. The potential energy of the work done by external forces, W , may be expressed in discrete form by

$$W = X^* F \quad (54)$$

where F is the vector of external forces. As the strain expressions are of second order in the displacement components, the total potential energy, V , of the shell is a polynomial of 4th degree in the discrete displacement unknowns. It is given by

$$V = U - W \quad (55)$$

A necessary condition for static equilibrium is that the potential energy be stationary. For a polynomial, this requires that the gradient of V vanishes and leads to the equation

$$LX = F \quad (56)$$

Here L is defined as the nonlinear operator such that

$$LX = \text{Grad } U \quad (57)$$

The derivation of the complete nonlinear solution of Eq. (56) as well as of bifurcation buckling is facilitated by introduction of the concept of the derivative L' of L (Ref. 10). In particular, for the operator L , the derivative L' (sometimes called the Frechet derivative of L) is an n -by- n matrix whose elements are

$$L'_{i,j} = \frac{\partial^2 U}{\partial X_{(i)} \partial X_{(j)}} \quad (58)$$

Because L' is a function of a particular displacement vector X (unless the nonlinear terms are dropped), the Frechet derivative will usually be denoted L'_X to indicate this dependence. With the use of the derivative L' of the operator L , Newton's method may be readily generalized to obtain the solution of Eq. (56). The iteration is defined by

$$L'^k_X (X_{k+1} - X_k) = F - LX_k \quad (59)$$

If X_0 is an estimate sufficiently close to the solution X and if L'_X is not a singular matrix, the iteration converges to X . Under these assumptions, it also can be shown that the converged solution is unique (Ref. 10).

2.7 Bifurcation Buckling

The application of Newton's method and the modified Newton method in STAGS to obtain a nonlinear collapse analysis is discussed in the previous section. It is interesting to note that the mathematical characterization of bifurcation buckling also is provided by the generalized Newton method. Let X_0 be a solution of Eq. (56) under a given vector F of external forces. If every neighborhood of X_0 contains another vector Y which satisfies the equation

$$LY = F \quad (60)$$

then bifurcation is said to occur for the shell under the load F . From the previous remarks on the conditions for convergence of Newton's method to a unique solution, it follows that a necessary condition for bifurcation is that L'_{X_0} be a singular matrix, or

$$\det (L'_{X_0}) = 0 \quad (61)$$

Classical bifurcation buckling theory (with linear prebuckling analysis) may be easily obtained from Eq. (61). It is assumed that X_0 may be written

$$X_0 = \lambda X_L \quad (62)$$

where X_L is the linear solution for a load vector F_L . Thus, Eq. (61) becomes

$$\det \left(L'_{\lambda X_L} \right) = 0 \quad (63)$$

Equation (63) is an algebraic eigenvalue problem of the form

$$\det (A - \lambda B - \lambda^2 C) = 0 \quad (64)$$

In classical bifurcation theory, the C matrix, which arises from the pre-buckling rotations, is often omitted and the eigenvalue problem

$$AX = \lambda BX \quad (65)$$

is obtained.

When bifurcation is considered but the prebuckling displacements are not linear, the solution of Eq. (61) generally requires a stepwise procedure. One such method is given by the recurrence equations

$$\det \begin{pmatrix} L'_{\lambda_{k+1}} & X_k \end{pmatrix} = 0 \quad (66)$$
$$X_{k+1} = \lambda_{k+1} X_k$$

in which the starting vector X_0 may be represented by the linear solution.

A sequence of eigenvalue problems is solved and, if the method is successful, λ_k approaches unity. A nonlinear bifurcation treatment [equivalent to Eq. (66)] was presented in Reference 11 and has been used successfully to study a large variety of problems. For the two-dimensional problems under consideration here, it appears that such methods may be as costly as the complete nonlinear analysis available in STAGS. Consequently, only a classical bifurcation buckling analysis is implemented in the STAGS program.

The formation of the A and B matrices of Eq. (65) will be considered briefly. The elements of the Frechet derivative matrix $L'_{\lambda X L}$ (which define the matrices A and B) are determined according to Eq. (58). The rules for computing derivatives of polynomials are easily programmed,

and the formation of the A and B matrices, therefore, is well suited to automatic treatment on the computer. Thus, for example, if $X_{(i)}$ and $X_{(j)}$ are the i^{th} and j^{th} displacement components, we have, using Eqs. (52), (53), and (54):

$$\frac{\partial^2 U}{\partial X_{(i)} \partial X_{(j)}} = \sum_{k=1}^m a^k \frac{\partial^2 \Delta U^k}{\partial X_{(i)} \partial X_{(j)}} \quad (67)$$

Examining the k^{th} term of this sum,

$$\frac{\partial^2 \Delta U^k}{\partial X_{(i)} \partial X_{(j)}} = \frac{\partial^2 Z^{k*}}{\partial X_{(i)} \partial X_{(j)}} \lambda S^k + \frac{\partial Z^{k*}}{\partial X_{(i)}} D^k \frac{\partial Z^k}{\partial X_{(j)}} \quad (68)$$

In the first term on the right-hand side of Eq. (68), note that S^k is the linear stress resultant vector at station k and that only the quadratic terms (rotations) need be considered in forming the partial derivatives $\partial^2 Z^{k*} / \partial X_{(i)} \partial X_{(j)}$. Contributions from this term go into the B matrix. Assuming the prebuckling rotations may be neglected for the classical theory, the last term of Eq. (68) generates additions only to the A matrix. The A matrix is then identical to the linear stiffness matrix. If the prebuckling rotations are included (nonlinear bifurcation), the last term of Eq. (68) generates a C matrix and provides additional contributions to the B matrix. In this case, the prebuckling stress resultant vector S would also include nonlinear terms.

In conclusion, it should be noted that bifurcation buckling theory is often based on the concept of adjacent equilibrium states. Of course, the same algebraic eigenvalue problem is ultimately obtained by both methods. However, the approach presented here seems to provide a more simple recipe for definition of the basic matrices of Eq. (65). The recipe is outlined in Eqs. (67) and (68) and leads to straightforward algebraic procedures. In addition, the relations between linear and nonlinear bifurcation theory and Newton's method are clarified.

2.8 Computation of the Components of the Metric and Curvature Tensors

The components of the metric tensor A, B, C and of the curvature tensor $b_{\alpha\beta}$ can be computed according to the following sequence of operations:

- 1) Denote the cartesian coordinates x^1, x^2, x^3 by x, y, z , respectively, and the surface coordinates φ^1, φ^2 by ξ, η . The x, y, z are then determined as functions of ξ and η .

$$\begin{aligned} x &= x(\xi, \eta) \\ y &= y(\xi, \eta) \\ z &= z(\xi, \eta) \end{aligned} \tag{69}$$

- 2) The metric tensor components are computed with the aid of Eqs. (4, 7)

$$\begin{aligned} A^2 &= a_{\xi\xi} = \left(\frac{\partial x}{\partial \xi}\right)^2 + \left(\frac{\partial y}{\partial \xi}\right)^2 + \left(\frac{\partial z}{\partial \xi}\right)^2 \\ B^2 &= a_{\eta\eta} = \left(\frac{\partial x}{\partial \eta}\right)^2 + \left(\frac{\partial y}{\partial \eta}\right)^2 + \left(\frac{\partial z}{\partial \eta}\right)^2 \end{aligned} \tag{70}$$

$$C = AB \cos \theta = a_{\xi\eta} = \frac{\partial x}{\partial \xi} \frac{\partial x}{\partial \eta} + \frac{\partial y}{\partial \xi} \frac{\partial y}{\partial \eta} + \frac{\partial z}{\partial \xi} \frac{\partial z}{\partial \eta}$$

- 3) The components of the curvature tensor are

$$\begin{aligned} b_{\xi\xi} &= \frac{\partial^2 x}{\partial \xi^2} k_{23} + \frac{\partial^2 y}{\partial \xi^2} k_{31} + \frac{\partial^2 z}{\partial \xi^2} k_{12} \\ b_{\xi\eta} &= \frac{\partial^2 x}{\partial \xi \partial \eta} k_{23} + \frac{\partial^2 y}{\partial \xi \partial \eta} k_{31} + \frac{\partial^2 z}{\partial \xi \partial \eta} k_{12} \\ b_{\eta\eta} &= \frac{\partial^2 x}{\partial \eta^2} k_{23} + \frac{\partial^2 y}{\partial \eta^2} k_{31} + \frac{\partial^2 z}{\partial \eta^2} k_{12} \end{aligned} \tag{71}$$

Contraits

where

$$\begin{aligned}k_{12} &= \frac{1}{\sqrt{a}} \left(\frac{\partial x}{\partial \xi} \frac{\partial y}{\partial \eta} - \frac{\partial x}{\partial \eta} \frac{\partial y}{\partial \xi} \right) \\k_{23} &= \frac{1}{\sqrt{a}} \left(\frac{\partial y}{\partial \xi} \frac{\partial z}{\partial \eta} - \frac{\partial y}{\partial \eta} \frac{\partial z}{\partial \xi} \right) \\k_{31} &= \frac{1}{\sqrt{a}} \left(\frac{\partial z}{\partial \xi} \frac{\partial x}{\partial \eta} - \frac{\partial z}{\partial \eta} \frac{\partial x}{\partial \xi} \right) \\a &= a_{\xi\xi} a_{\eta\eta} - a_{\xi\eta}^2\end{aligned}\tag{72}$$

Since the sign of the curvature tensor was chosen so that positive curvature results from an inward point unit normal [see Eq. (19)], care must be taken to preserve the sense of $b_{\alpha\beta}$ by remembering that it is defined by the cross product $a_{\xi} \times a_{\eta}$.

As an example, consider the case of an elliptic cone as shown in Figure 2. The parameters α and β are the tangents of the cone half apex angles in the x-z and y-z planes, respectively, ξ is the elliptic coordinate, and η is the axial coordinate. The relationships between x, y, z and ξ, η are

$$\begin{aligned}x &= \alpha \eta \cos \xi \\y &= \beta \eta \sin \xi \\z &= \eta\end{aligned}\tag{73}$$

Note that this choice of ξ and η results in an outward pointing normal as shown in Figure 2.

The $a_{\alpha\beta}$ and $b_{\alpha\beta}$ are computed from Eqs. (70, 71)

$$a_{\xi\xi} = \eta^2 (\alpha^2 \sin^2 \xi + \beta^2 \cos^2 \xi) + 1$$

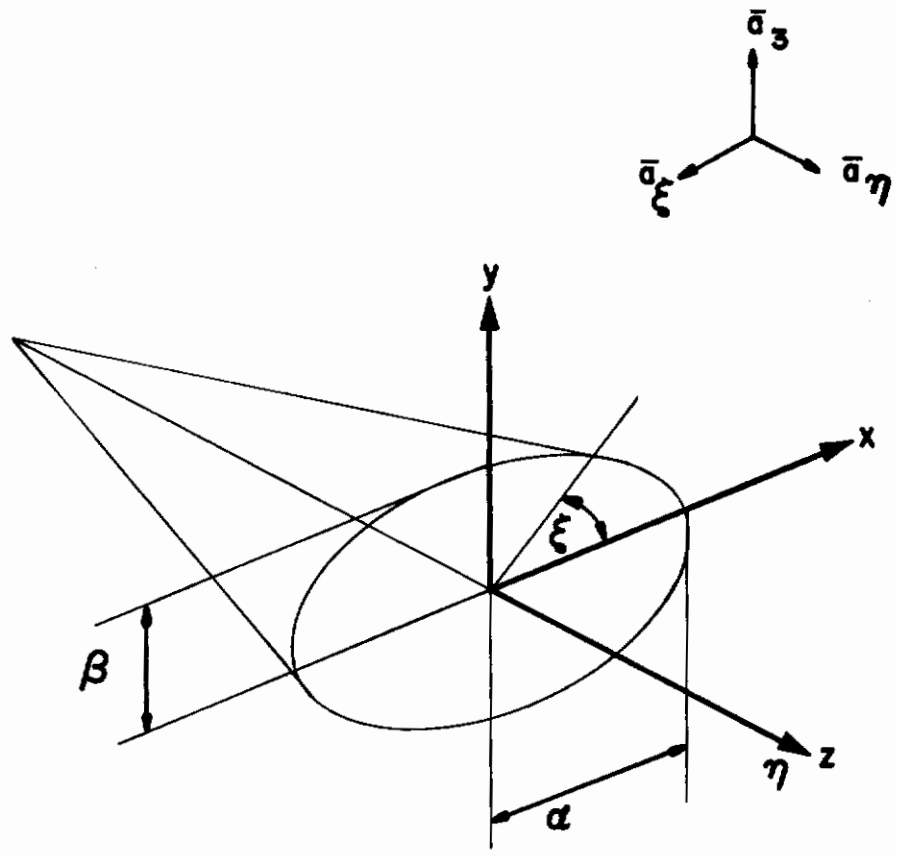


Figure 2 An Elliptic Cone

$$\begin{aligned}
 a_{\xi\eta} &= \eta(\beta^2 - \alpha^2) \sin \xi \cos \xi \\
 a_{\eta\eta} &= \alpha^2 \cos^2 \xi + \beta^2 \sin^2 \xi \\
 b_{\xi\xi} &= -\frac{1}{\sqrt{a}} \alpha \beta \eta^2 \\
 b_{\xi\eta} &= 0 \\
 b_{\eta\eta} &= 0 \\
 a &= \eta^2 (\alpha^2 \sin^2 \theta + \beta^2 \cos^2 \theta + \alpha^2 \beta^2)
 \end{aligned}
 \tag{74}$$

2.9 Physical Components of Strain and Curvature-Change

For lines of curvature coordinates, the physical components of strain and curvature-change are given by

$$\begin{aligned}
 \epsilon_{(\alpha\beta)} &= \frac{\epsilon_{\alpha\beta}}{\sqrt{a_{\alpha\alpha} a_{\beta\beta}}} && \text{(no sum)} \\
 \kappa_{(\alpha\beta)} &= \frac{\kappa_{\alpha\beta}}{\sqrt{a_{\alpha\alpha} a_{\beta\beta}}} && \text{(no sum)}
 \end{aligned}
 \tag{75}$$

With the components of the metric and curvature tensors written as

$$\begin{aligned}
 \alpha_1 &= \sqrt{a_{11}} \\
 \alpha_2 &= \sqrt{a_{22}} \\
 \frac{1}{r_1} &= \frac{b_{11}}{a_{11}} \\
 \frac{1}{r_2} &= \frac{b_{22}}{a_{22}}
 \end{aligned}
 \tag{76}$$

The physical components of the displacement gradients (Eq. (36)) take the form

$$\begin{aligned}
 \gamma_{(11)} &= \frac{1}{\alpha_1} u_{(1),1} + \frac{\alpha_{1,2}}{\alpha_1 \alpha_2} u_{(2)} - \frac{w}{r_1} \\
 \gamma_{(12)} &= \frac{1}{\alpha_2} u_{(1),2} - \frac{\alpha_{2,1}}{\alpha_1 \alpha_2} u_{(2)} \\
 \gamma_{(21)} &= \frac{1}{\alpha_1} u_{(2),1} - \frac{\alpha_{1,2}}{\alpha_1 \alpha_2} u_{(1)} \\
 \gamma_{(22)} &= \frac{1}{\alpha_2} u_{(2),2} + \frac{\alpha_{2,1}}{\alpha_1 \alpha_2} u_{(1)} - \frac{w}{r_2} \\
 \beta_{(1)} &= \frac{1}{\alpha_1} w_{,1} + \frac{1}{r_1} u_{(1)} \\
 \beta_{(2)} &= \frac{1}{\alpha_2} w_{,2} + \frac{1}{r_2} u_{(2)}
 \end{aligned} \tag{77}$$

where a comma denotes partial differentiation and the quantities $u_{(\alpha)}$ are the physical components of displacement in the φ^α directions.

The physical components of strain and curvature-change are determined from Eqs. (42) and are found to be

$$\begin{aligned}
 \epsilon_{(11)} &= \gamma_{(11)} + \frac{1}{2} \gamma_{(11)}^2 + \frac{1}{2} \gamma_{(21)}^2 + \frac{1}{2} \beta_{(1)}^2 \\
 \epsilon_{(12)} &= \frac{1}{2} (\gamma_{(12)} + \gamma_{(21)}) + \frac{1}{2} \gamma_{(11)} \gamma_{(12)} + \frac{1}{2} \gamma_{(21)} \gamma_{(22)} + \frac{1}{2} \beta_{(1)} \beta_{(2)} \\
 \epsilon_{(22)} &= \gamma_{(22)} + \frac{1}{2} \gamma_{(12)}^2 + \frac{1}{2} \gamma_{(22)}^2 + \frac{1}{2} \beta_{(2)}^2
 \end{aligned} \tag{78}$$

Contrails

$$n_{(11)} = \frac{1}{\alpha_1} \beta_{(1),1} + \frac{1}{\alpha_1 \alpha_2} \alpha_{1,2} \beta_{(2)} - \frac{1}{r_1} \gamma_{(22)}$$

$$n_{(12)} = n_{(21)} = \frac{1}{\alpha_1} \beta_{(2),1} - \frac{1}{\alpha_1 \alpha_2} \alpha_{1,2} \beta_{(1)} + \frac{1}{r_1} \gamma_{(12)}$$

(79)

$$= \frac{1}{\alpha_2} \beta_{(1),2} - \frac{1}{\alpha_1 \alpha_2} \alpha_{2,1} \beta_{(2)} + \frac{1}{r_2} \gamma_{(21)}$$

$$n_{(22)} = \frac{1}{\alpha_2} \beta_{(2),2} + \frac{1}{\alpha_1 \alpha_2} \alpha_{2,1} \beta_{(1)} - \frac{1}{r_2} \gamma_{(11)}$$

Section 3.0

FINITE DIFFERENCE GRID WITH VARIABLE SPACING

For better economy in the analysis a capability has been provided for the use of variable spacing finite difference grids. The shell surface is covered with a system of mesh lines (see Fig. 3) whose coordinates are given by

$$x_i, \quad i = 1, m$$

and

$$y_j, \quad j = 1, n$$

where x and y are the curvilinear surface coordinates. Corresponding to each pair of values (i, j) $i = 1, m; j = 1, n$, a rectangular region $R_{i,j}$ is defined with sides of length

$$a_{i,j} = 1/2 |x_{i+1} - x_{i-1}|$$

$$b_{i,j} = 1/2 |y_{j+1} - y_{j-1}|$$

Note that $R_{i,j}$ is rectangular on the map of the shell provided by the surface coordinates but not generally on the shell itself.

The regions $R_{i,j}$ (and lengths $a_{i,j}, b_{i,j}$) are modified at boundaries of a shell by including only those portions which are inside the panel. A double integral of a function f over the region R of the panel may then be approximated by

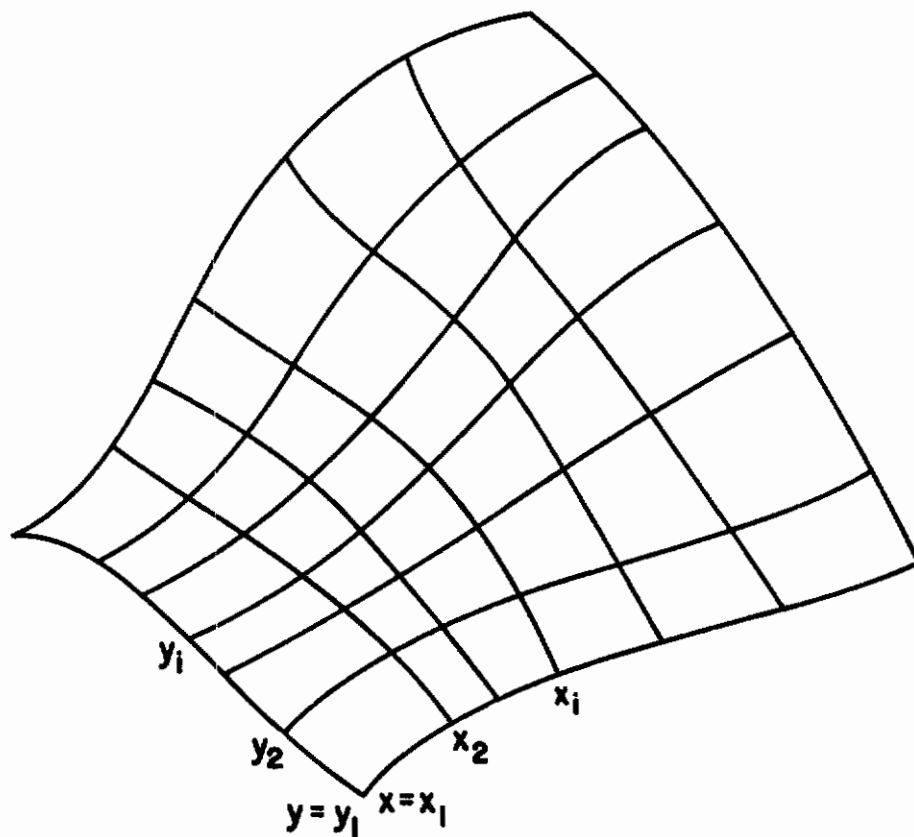


Figure 3 Shell Surface Covered With A System of Mesh Lines

$$\iint_R f \, dx dy = \sum_{i=1}^m \sum_{j=1}^n f_{i,j} a_{i,j} b_{i,j} \quad (80)$$

The discretization is completed when the integrand functions $f_{i,j}$ are evaluated at the centroids of the regions $R_{i,j}$ in terms of the neighboring displacement components. It should first be noted that the tangential displacements u and v have been located at corners of the regions $R_{i,j}$. Furthermore, the energy expressions for a shell include derivatives of u and v only up to the first order. Hence, even with arbitrary spacing, only central difference formulas for the u and v displacements are required. In contrast, the normal displacement w has been located at the mesh node points (x_i, y_j) and more general finite difference formulas must be developed.

The coordinates of the centroid of a region $R_{i,j}$ are given by

$$\begin{aligned} \tilde{x}_i &= 1/4 (x_{i-1} + 2x_i + x_{i+1}) \\ \tilde{y}_j &= 1/4 (y_{j-1} + 2y_j + y_{j+1}) \end{aligned} \quad (81)$$

Variable spacing is first considered with respect to a single coordinate x only. With the help of a Taylor's expansion (or equivalently by the use of interpolation formulas), the difference formulas for w , w_x and w_{xx} at \tilde{x}_i may be established as

$$\begin{aligned} (w)_i \equiv w|_{\tilde{x}_i} &= w_{i-1}/16 \cdot [(h-k) \cdot (3k+h)/(h^2 + hk)] \\ &+ w_i/16 \cdot [(h+3k) \cdot (3h+k)/(h+k)] \\ &+ w_{i+1}/16 \cdot [(k-h) \cdot (3h+k)/(hk+k^2)] \end{aligned} \quad (82)$$

$$\begin{aligned}
 (w, x)_i &\equiv w, x \Big|_{\tilde{x}_i} = -w_{i-1}/(2h) \\
 &+ w_i [1/(2h) - 1/(2k)] \\
 &+ w_{i+1}/(2k)
 \end{aligned} \tag{83}$$

$$\begin{aligned}
 (w, xx)_i &\equiv w, xx \Big|_{\tilde{x}_i} = w_{i-1} \cdot 2/[h \cdot (h+k)] \\
 &- w_i \cdot 2/(h \cdot k) \\
 &+ w_{i+1} \cdot 2/[k \cdot (h+k)]
 \end{aligned} \tag{84}$$

where

$$\begin{aligned}
 h &= x_i - x_{i-1} \\
 k &= x_{i+1} - x_i
 \end{aligned} \tag{85}$$

The corresponding formulas for the y coordinate are obtained by appropriate substitutions and are denoted with superscripts

$$\begin{aligned}
 (w)^j &\equiv w \Big|_{\tilde{y}_j} \\
 (w, y)^j &\equiv w, y \Big|_{\tilde{y}_j} \\
 (w, yy)^j &\equiv w, yy \Big|_{\tilde{y}_j}
 \end{aligned} \tag{86}$$

The required two-dimensional difference formulas are now obtained

by combining the formulas for both coordinate directions

$$\begin{aligned} \tilde{w}_{i,j} &\equiv w|_{(\tilde{x}_i, \tilde{y}_j)} = ((w)_i)^j = ((w)^j)_i \\ \tilde{w}, \tilde{xx}_{i,j} &\equiv w, xx|_{(\tilde{x}_i, \tilde{y}_j)} = ((w, xx)_i)^j \\ \tilde{w}, \tilde{yy}_{i,j} &\equiv w, yy|_{(\tilde{x}_i, \tilde{y}_j)} = ((w, yy)_i)^j \\ \tilde{w}, \tilde{xy}_{i,j} &\equiv w, xy|_{(\tilde{x}_i, \tilde{y}_j)} = ((w, xy)_{i,y})^j \end{aligned} \tag{87}$$

In general, these equations involve the 9 point "star" of neighboring values. However, it is easily seen that all of the formulas reduce to the standard central difference formulas when uniform rectangular spacing is used. All of the difference formulas are exact when the displacement function w behaves quadratically

The inclusion of nonorthogonal coordinates and of variable grid spacing extends considerably the class of cases that can be solved by use of STAGS. The grid lines can be made to follow boundary lines and cutout edges rather than lines of curvature on the shell surface. As an example, for a cylinder with a circular cutout, one can use a grid as shown in Figure 4. This grid system is described by the mapping function

$$f(x) = a(1-x) + \frac{\pi R x}{M}$$

$$g(x) = b(1-x) + Lx$$

$$F = \left\{ [f \sin \phi] \frac{2}{1-x} + [g \cos \phi] \frac{2}{1-x} \right\} \frac{1-x}{2}$$

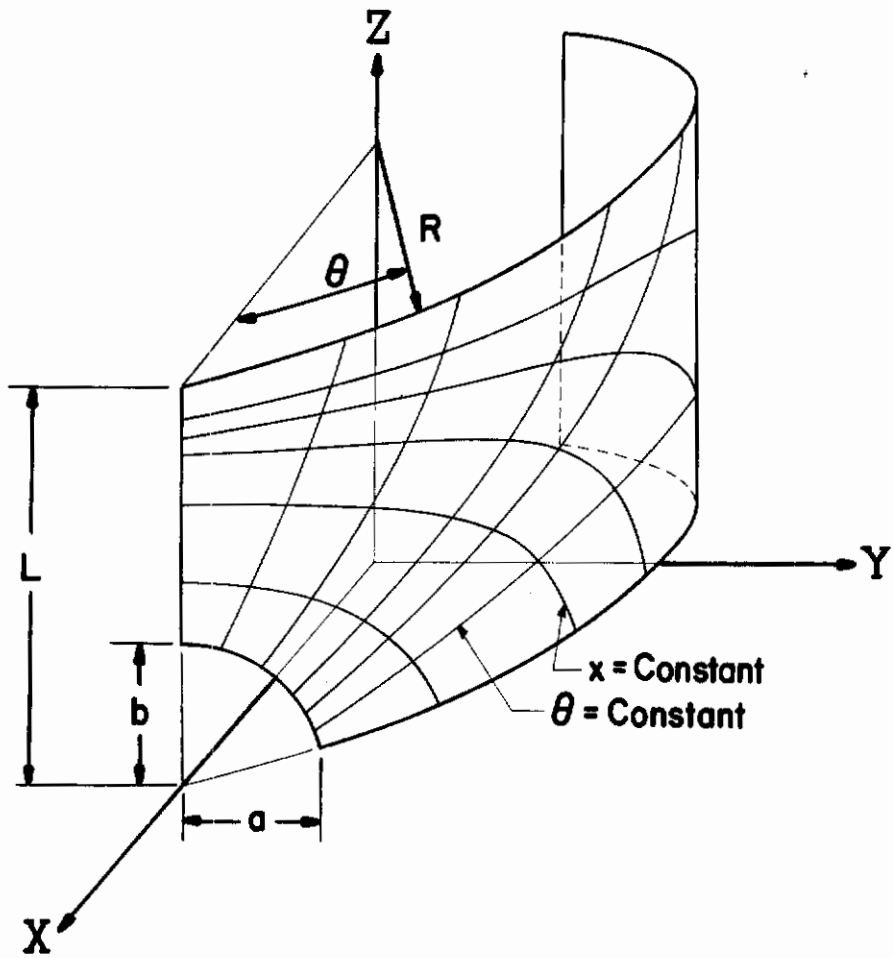


Figure 4 Grid for Cylinder With Circular Cutout

$$X = R \sin [F \cos \phi / R] \quad (88)$$

$$Y = R \cos [F \cos \phi / R]$$

$$Z = F \sin \phi$$

However, it was found that use of this grid leads to inaccurate results unless the spacing between the straight gridlines are very close together in the neighborhood of the corner. The reason for this is that the equations for the strains are inaccurate if the angle between the coordinates changes significantly between two adjacent gridpoints. It appears to be more practical, until other finite difference expressions have been developed, to use a different approach. For shells with cutouts that cannot easily be made to follow a regular net, it is suggested that the user written subroutine for a variable thickness shell be used. The shell thickness is set equal to zero if a gridpoint falls inside the cutout. The computer program then eliminates as unknowns the displacement components at points with zero thickness. This method is demonstrated in the example given in Section 5.3.

Section 4.0 INELASTIC BEHAVIOR

4.1 Introduction

Due to the extreme complexity of the problem, it has been necessary to formulate theories of plasticity which greatly simplify material behavior. While in many cases these theories give satisfactory results, there are other cases in which they fail. It is shown, for instance, in Reference 12 that for loading histories with sharp turns in the stress space the classical theory with isotropic strain hardening may give very poor results. Typically at collapse there is a very sharp change in deformation pattern and, consequently, a sharp turn in the stress path. Other theories have been proposed which more adequately describe the material behavior in such cases than does the classical theory. The Batdorf-Budiansky slip theory (Ref. 13) is probably too cumbersome for practical application, but the type of theory proposed by White (Ref. 14) and Besseling (Ref. 15) appears very promising because it is rather simple in its application, yet it retains such features as strain hardening and the Bauschinger effect. For these reasons, it was selected for use in the STAGS code.

Introduction of inelastic behavior has been done within the framework of the energy principle upon which the elastic analysis was based. Essentially, the plastic deformations are considered as load terms; they are completely analogous to thermal expansions except that they are not known in advance. A series of elastic problems are solved by the use of energy principles in which the "load terms" are gradually modified until they correspond to the computed state of stress and to specified nonlinear stress strain relations at all points over the shell surface and through the shell thickness.

4.2 The White-Besseling Theory

The White-Besseling Theory, as applied here, assumes that the material consists of several components which have identical elastic properties and exhibit ideal plasticity (no strain hardening) but have different yield strength. As the strain is the same in all components, the stress-strain curve will experience a decrease in slope as the stress reaches the yield limit for any one of the components; the respective components then cease to take additional load. The composite thus exhibits strain hardening with a piecewise linear stress-strain relation. Use of only one component will, of course, result in application of ideal plasticity theory. If the stress is reversed after loading beyond the yield limit for one or more components, yield will occur in the reversed direction at an average stress in the composite which is lower than the stress for original yield. This is demonstrated in the uniaxial stress-strain curve shown in Figure 5. Tension is first applied, OAB, beyond the yield limit and followed by strain reversal, BCD, into the zone of yield in compression. The yield ellipse for the weakest component and the loading history in this component are also shown in this figure. Clearly, yield in compression will occur when the total strain is $(\epsilon_1 - 2\epsilon_y)$, i. e., the yield in compression occurs at a much lower stress if the material previously has been subjected to tension stresses above the yield point. To introduce the Bauschinger effect this way is appealing because it reflects the microstress theory which now generally is accepted as the explanation of the Bauschinger effect.

4.3 Implementation of the White-Besseling Theory in STAGS

The White-Besseling plasticity theory is implemented in the computer program in the following manner:

- 1) The inelastic behavior of the material is defined through specification of the uniaxial stress-strain curve. This curve is piecewise linear and the input consists of stress and strain at each of its corners. The relative volume and the yield strength for each of the components is then computed internally. The transverse strain is determined such that the

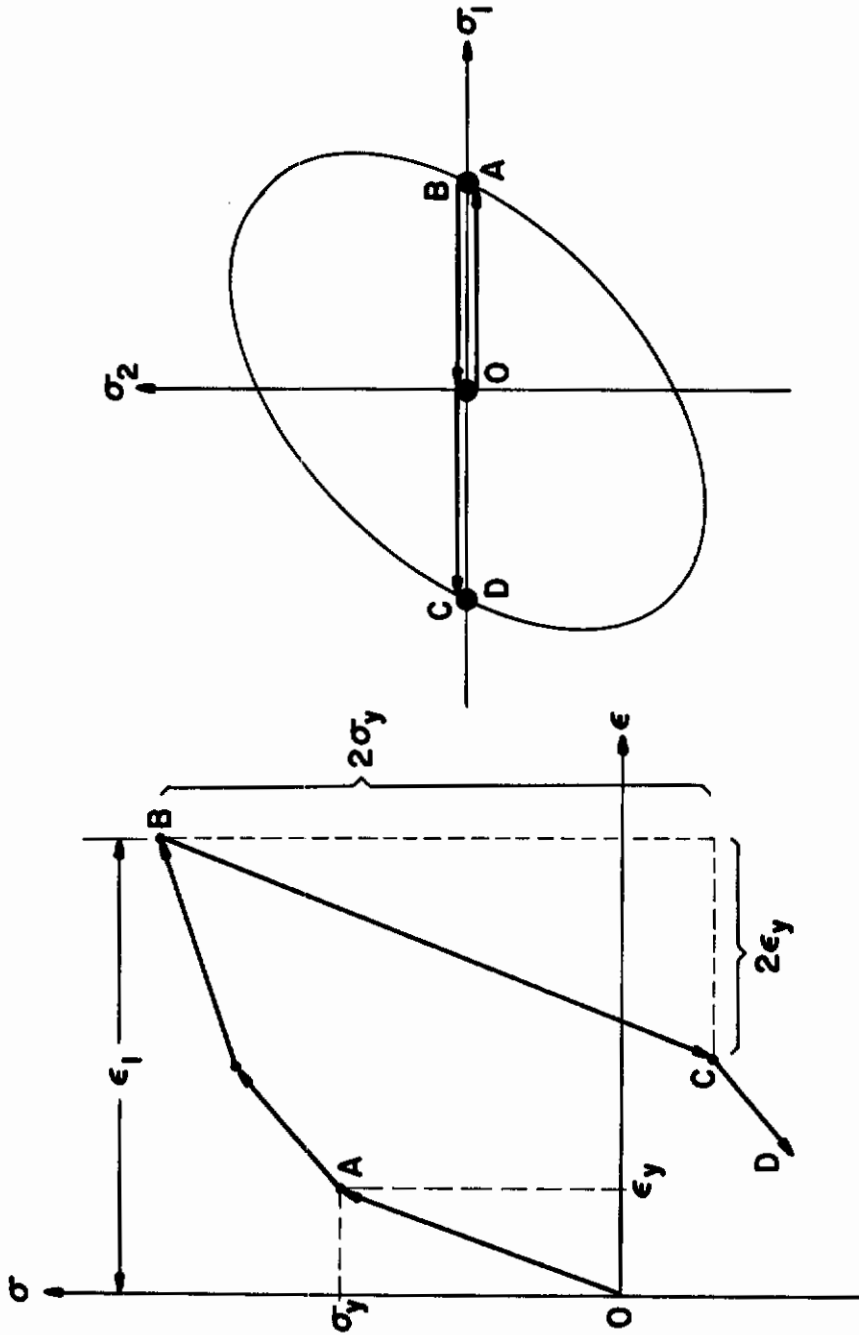


Figure 5 Stress Strain Curve Showing Bauschinger Effect

total stress in the transverse direction is zero. It seems possible to reflect more accurately the actual stress-strain relations, including anisotropy, if self-equilibrating initial stresses are included.

(2) The strains are estimated for all points in the shell over the shell coordinates and through the thickness. This generally is done through extrapolation from previous solutions.

(3) A subroutine is called within which, for each of the material components, the stress corresponding to the assumed strains is determined. The total stress for the composite is then found.

$$\sigma_{\text{total}} = \sum_{i=1}^J v_i \sigma_i$$

where J is the number of components, v_i is the relative volume occupied by component number i , $\left(\sum_{i=1}^J v_i = 1.0\right)$, and σ_i is the yield stress for component number i .

(4) Once total strains and stresses are known, the plastic part of the strain increment can be determined and added as a pseudo-load in an elastic analysis.

(5) New strains are computed and used as estimates. The procedure is continued until the computer strains agree to within a given margin with the estimated strains.

The following operations are performed in the above referenced subroutine:

(1) Information about material properties is transferred into the subroutine together with the estimated strain increments ($\Delta\epsilon_1$, $\Delta\epsilon_2$, and $\Delta\gamma$) and stresses at the end of the previous load step ($\tilde{\sigma}_1$, $\tilde{\sigma}_2$, γ).

(2) New stresses are computed under the assumption that the load step is elastic.

$$\begin{aligned}\sigma_1 &= \tilde{\sigma}_1 + \frac{E}{1-\nu^2} (\Delta\epsilon_1 + \nu\Delta\epsilon_2) \\ \sigma_2 &= \tilde{\sigma}_2 + \frac{E}{1-\nu^2} (\Delta\epsilon_2 + \nu\Delta\epsilon_1)\end{aligned}\tag{89}$$

$$\tau = \tilde{\tau} + E\Delta\gamma/[2(1+\nu)]$$

$$(3) \quad \text{Set } \sigma_T = \sigma_1^2 + \sigma_2^2 - \sigma_1 \sigma_2 + k^2 \tau^2 \quad (90)$$

where k is the ellipse ratio for the assumed yield surface (usually, $k^2 = 3$).

(4) If σ_T is less than σ_Y^2 , the load step is elastic in this component (loading or unloading). If this is the case for all components, there are no pseudo loads caused by plastic strain increments and the calculations for the load step are concluded.

(5) If σ_T is larger than σ_Y^2 for some component, the step is at least partly inelastic for this component. As we have assumed ideal plasticity the stresses can be computed from the conditions that

$$\sigma_1^2 + \sigma_2^2 - \sigma_1 \sigma_2 + k^2 \tau^2 = \sigma_Y^2 \quad (91)$$

where

$$\begin{aligned} \sigma_1 &= \tilde{\sigma}_1 + \frac{E}{1-\nu} \left[\Delta \epsilon_1 - \Delta \epsilon_1^P + \nu (\Delta \epsilon_2 - \Delta \epsilon_2^P) \right] \\ \sigma_2 &= \tilde{\sigma}_2 + \frac{E}{1-\nu} \left[\Delta \epsilon_2 - \Delta \epsilon_2^P + \nu (\Delta \epsilon_1 - \Delta \epsilon_1^P) \right] \\ \tau &= \tilde{\tau} + \frac{E}{2(1+\nu)} \left[\Delta \gamma - \Delta \gamma^P \right] \end{aligned} \quad (92)$$

and that the plastic flow is perpendicular to the yield surface

$$\frac{\Delta \epsilon_1^P}{\Delta \epsilon_2^P} = \frac{2\tilde{\sigma}_1 - \tilde{\sigma}_2}{2\tilde{\sigma}_2 - \tilde{\sigma}_1} ; \quad \frac{\Delta \epsilon_1^P}{\Delta \gamma^P} = \frac{2\tilde{\sigma}_1 - \tilde{\sigma}_2}{2k^2 \tilde{\tau}} \quad (93)$$

After the stresses have been determined in the components, the average stress in the composite is found readily. As the elastic constants are the same for all components, the plastic part of the strain increment (i. e., the pseudo loads), can easily be obtained.

The acquired ability to handle cases with inelastic behavior is demonstrated in one of the examples discussed in the following section.

Section 5.0

RESULTS OF SAMPLE CASES

In the following section are presented some numerical results obtained through exercise of the program. The examples were chosen such that the recent additions to the program could be verified.

5.1 Cylinder With Rectangular Cutout

Analytical and experimental results for cylindrical shells with rectangular cutouts were reported earlier in Reference 3. The benefit derived from the use of a variable mesh spacing has been evaluated by re-examining this cylinder problem. The cylinder has two diametrically opposite cutouts and a radius-to-thickness ratio of 400. It was reported in Reference 3 that a reasonably accurate analysis for such cylinders would require excessive computer time. Numerical results for a uniform finite difference net with 9 points in the axial and 20 points (9×20) in the circumferential direction (also presented in Ref. 3) are shown here in Figure 6. Due to improvements in the efficiency of the computer program, it is now possible to obtain much better results even with constant grid spacing. Curve B is obtained with a finer net (16×20). A finite difference mesh was designed also in which the minimum grid spacing is identical to that used for Curve B, but which gradually increases away from the cutout until it is approximately doubled. The displacements corresponding to this analysis are practically identical to those obtained by use of grid with constant spacing, but the computer time is reduced by about 40%.

Curve C was determined by use of a minimum grid spacing of 0.2 inch at the edge of the cutout. Moving away from the cutout the spacing increases by a factor of 1.2 from one mesh to the next until the maximum grid size of 0.6 inch is obtained. For Curve D the minimum size is 0.12

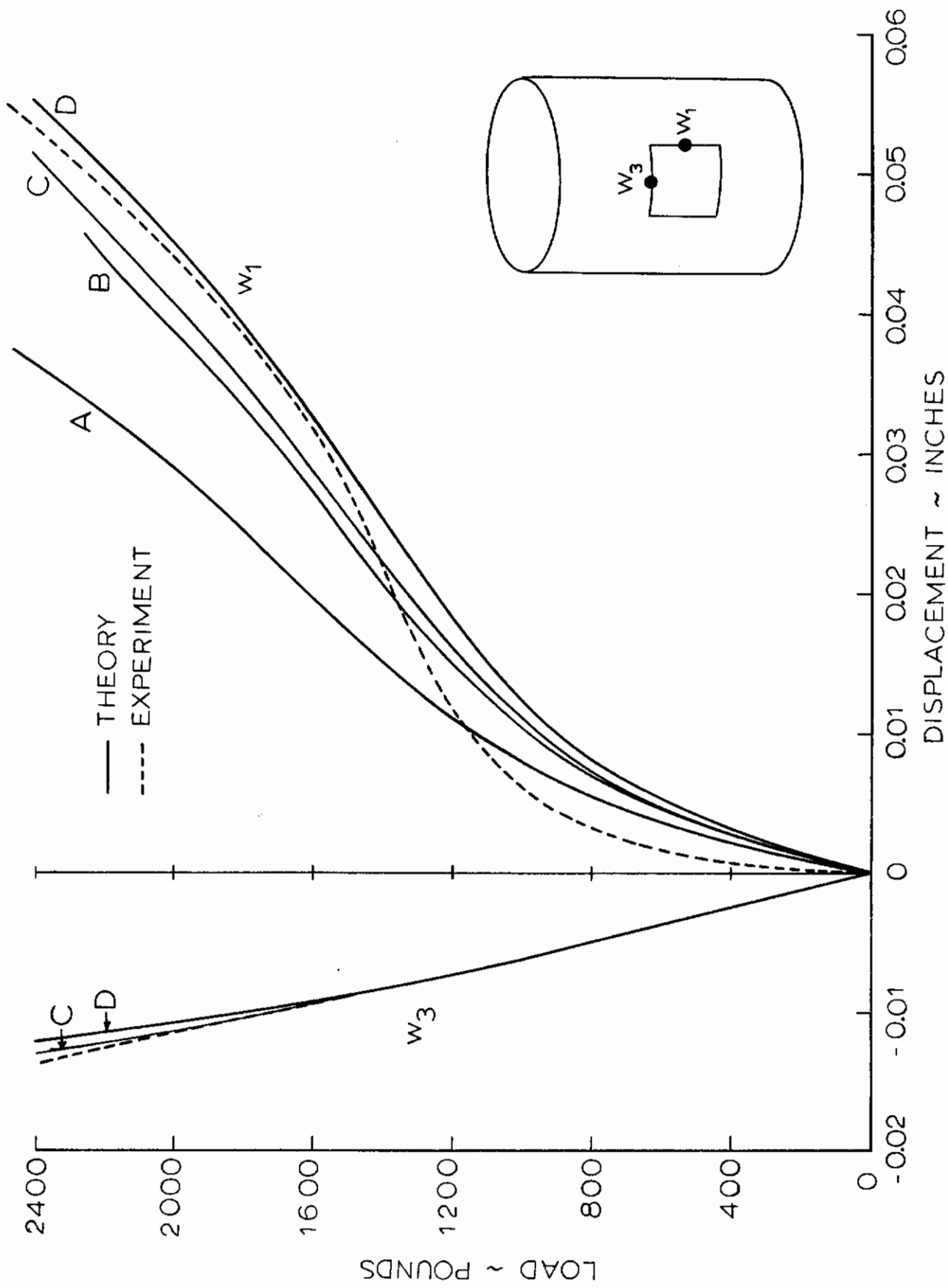


Figure 6 Load Displacement Curves for a Circular Cylindrical Shell with Cutouts

inch, the factor is 1.5 and the maximum size is again 0.6 inch. The results obtained by use of the latter mesh appear to be in very good agreement with the experimental results. The computer time corresponding to the determination of one of these curves is approximately 0.5 hours (UNIVAC 1108). For analyses with even finer mesh sizes, therefore, the analysis was restricted to loads below 845 pounds. The results in Table I show that additional refinement of the mesh would not substantially change the results shown in Curve D.

Table I
Displacement w_1 at $P = 845$ lbs

Net	Min. Spacing	Factor	Max. Spacing	w_1
D (13 x 21)	.12	1.5	.60	.00877
E (18 x 25)	.12	1.2	.60	.00850
F (21 x 35)	.12	1.2	.30	.00858
G (21 x 28)	.08	1.2	.60	.00873

5.2 The Pinched Cylinder

The case of a pinched cylinder, Figure 7, was also analyzed to further demonstrate the advantages of the variable grid capability. Lateral displacements computed from a linear analysis are shown versus the circumferential coordinate in Figure 8 and versus the axial coordinate in Figure 9. The curves are for a converged solution, corresponding to a variable spacing grid with 17 points in the axial and 26 points in the circumferential directions (17 x 26). These results are in good agreement with results for the same case shown in Reference 16. Discrete values of the solution are given for the two coarser nets (A and B) which are shown in Figure 10. It can be seen that the use of the net with variable spacing, Grid A, leads to results which are at least of the same quality as those obtained with the uniform net, Grid B. The computer time corresponding to the analysis with Grid B is approximately five times the time for analysis with Grid A.

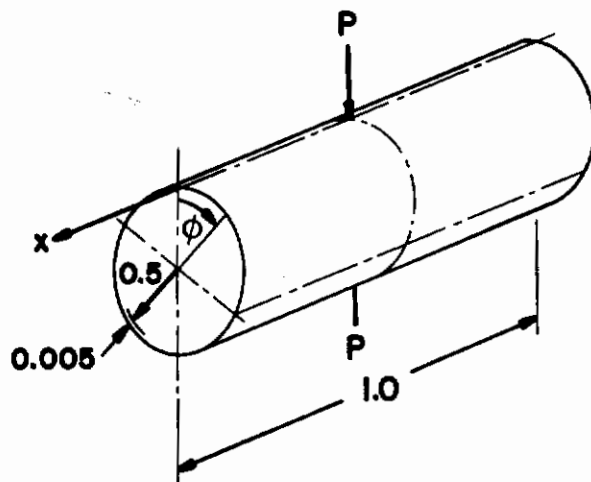


Figure 7 Pinched Cylinder

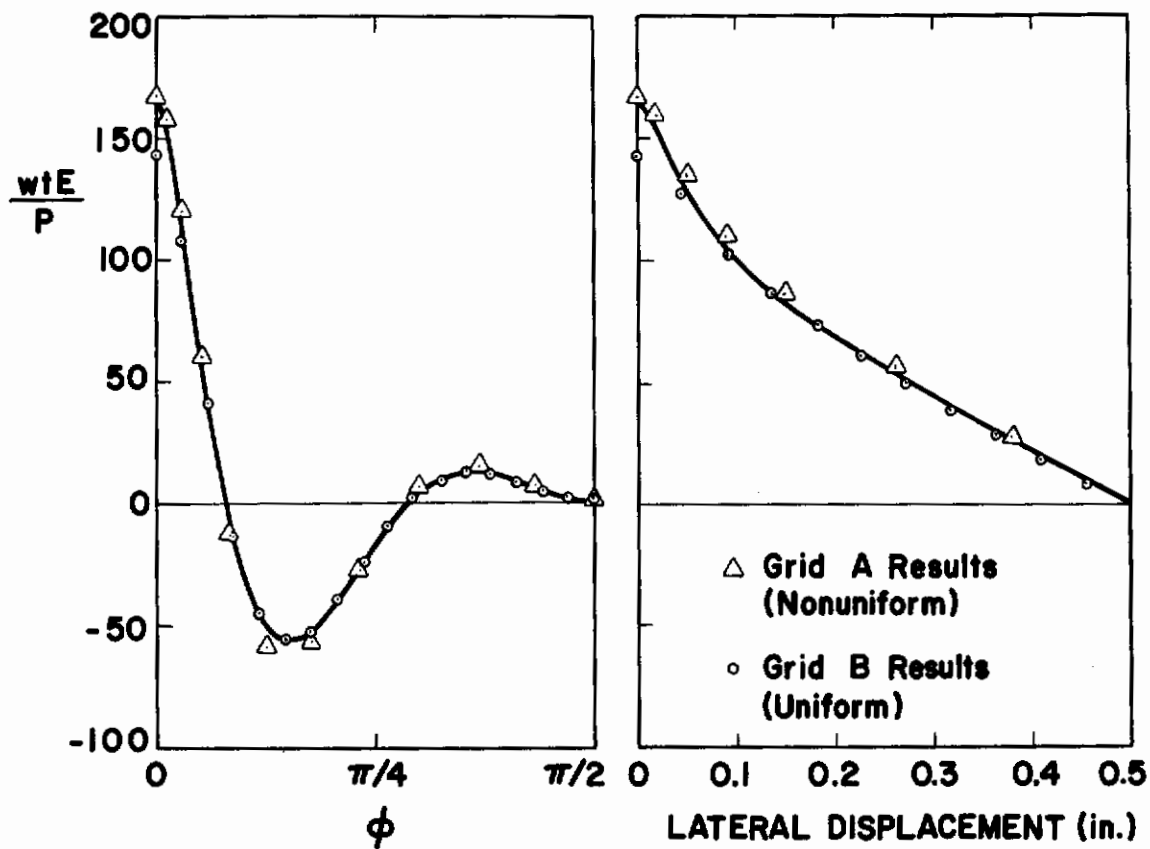
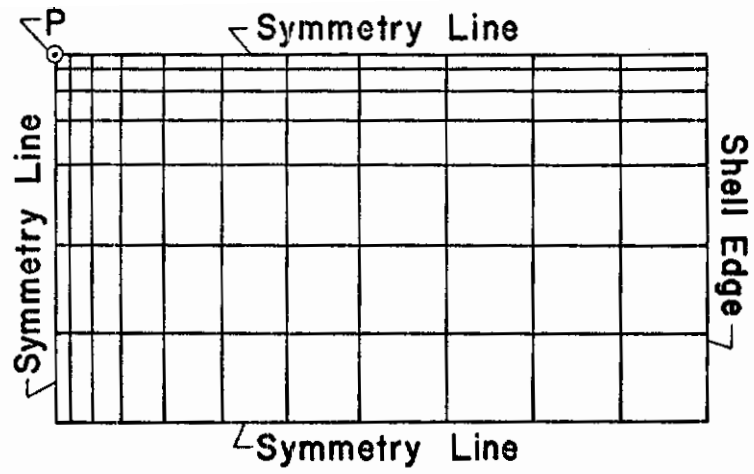
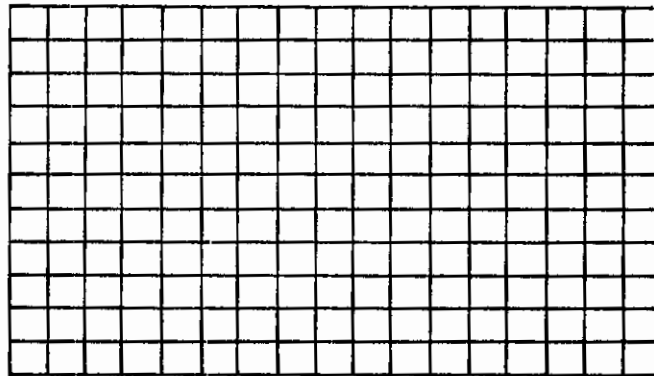


Figure 8 Lateral Displacement for Pinched Cylinder

Figure 9 Lateral Displacements for Pinched Cylinder



GRID A (8 x 12)



GRID B (12 x 18)

Figure 10 Finite Difference Grids

5.3 Cylinders With a Circular Cutout

A circular cylinder was analyzed for collapse under uniform end shortening. Its geometrical properties were: length 9 inches, radius 6 inches, thickness 0.06 inch. At its midlength, it had two diametrically opposite circular cutouts, each of radius 2.35 inches. Young's modulus was set to 10^7 psi and Poisson's ratio to 0.3. Due to symmetry, only half the length and one quarter of the circumference of the shell was considered. A finite difference net was chosen with 15 axial and 19 circumferential stations (15 x 19). The net is shown in Figure 11. The analysis indicates collapse (a maximum load) for an end shortening of .0209 inch. The load maximum is 16,740 lbs or 66,960 lbs for the complete cylinder.

The difference between the displacements for two adjacent solutions close to the point of collapse represents the collapse mode for the case. In Figure 12c is shown how these incremental displacements vary with the angular coordinate (see Fig. 11). Figure 12b shows the lateral displacement increments at the meridian $\theta = 57^\circ$. The displacements at the edge of the cutout ($\theta = 22.5^\circ$) and at $\theta = 57^\circ$ are shown as functions of the axial load in Figure 13. While the largest displacement occurs at the cutout edge, the displacement at $\theta = 57^\circ$ is growing faster indicating that "buckling" occurs away from the cutout where the axial stresses are higher.

5.4 Shells with Elliptic Cross-Section

For an elliptic cone the geometric constants occurring in the kinematic relations are given as an example in Section 2.8. These expressions were used here in an analysis of an elliptic cone with the dimensions shown in Figure 14.

Numerical results were first obtained for the special case of an elliptic cylinder with a length of 1.0 in., a thickness of 0.0144 in., and semi-axes of 1.75 in. and 1.0 in. (see Fig. 14). Young's modulus was 10^7 psi and Poisson's ratio was 0.3. The cylinder was subjected to a uniform end shortening with the edges free to rotate but restrained from moving in the radial and circumferential directions.

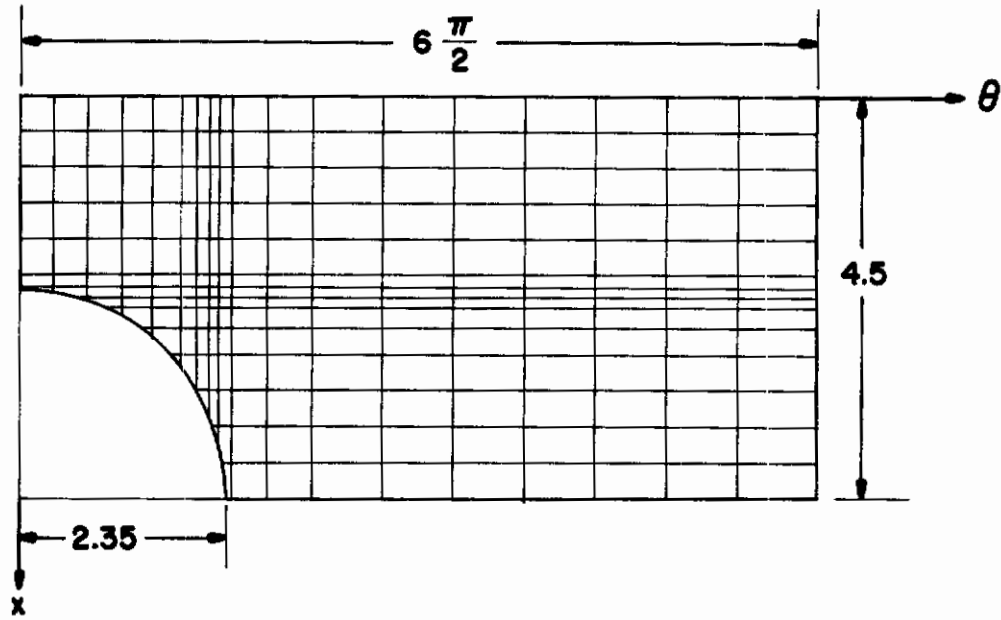


Figure 11 Finite Difference Grid For Cylinder With Circular Cutout

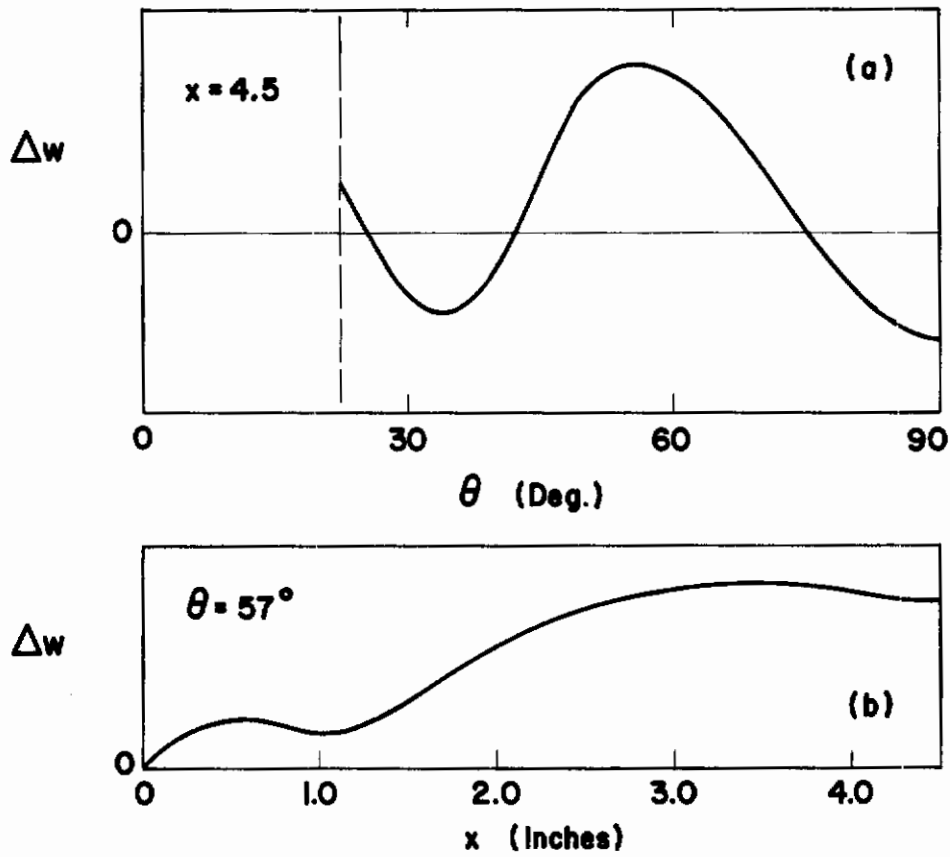


Figure 12 Collapse Modes for Cylinder With Circular Cutout

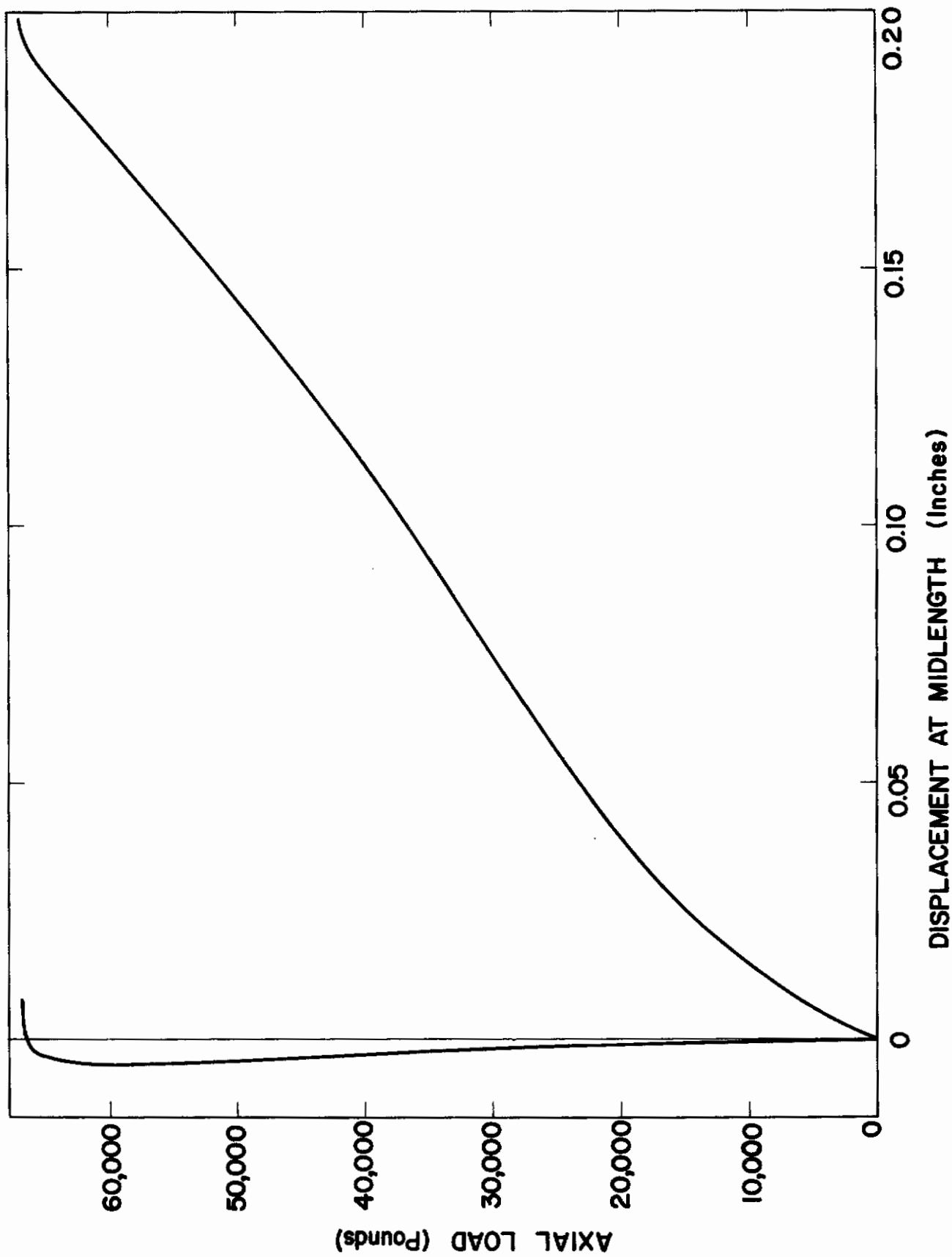


Figure 13 Load Displacement Curves for Cylinder with Circular Cutouts

Since the "buckling pattern" was expected to be confined to the areas of least curvature, it appeared that antisymmetric behavior with respect to the normal plane through $\varphi = 0$ (Fig. 14) could be excluded. Hence, the analysis was restricted to a 180° panel with symmetry conditions enforced at $\varphi = 0, \pi$. A uniform finite difference grid was chosen with 11 points in the axial and 29 points in the circumferential directions. Results obtained with finer grids indicated that use of the chosen grid led to accurate computations of the collapse load.

Due to the symmetry of the prebuckling deformation about the plane at midlength and about the normal plane through $\varphi = \pi/2$, it was necessary to excite nonsymmetric deformations by the use of small antisymmetric imperfections. Despite the presence of these imperfections, a deformation pattern developed at collapse which was symmetric about both of these planes. Therefore, the continued analysis was restricted to panels covering half the cylinder length and one quarter of the circumference.

For the particular cylinder considered (aspect ratio of 1.75), it is possible to determine the critical load without the use of symmetric (with respect to the geometric symmetry planes) imperfections. As the load is increased, a very sharp maximum is found in the load displacement curve (Figure 14). Beyond this maximum convergence cannot be obtained, hence the post-buckling curve cannot be directly determined.

For an imperfect shell, the displacement mode which developed at collapse for a perfect shell was used as a guide in the choice of a suitable initial imperfection mode

$$w = -w_0 \sin \left(\frac{\pi x}{L} \right) \cos (6 \theta)$$

Load displacement curves were computed for several different values of the imperfection amplitude w_0 . The results are shown in Figure 14. The normal displacement at $\varphi = \pi/2$, $x = L/2$ is shown as a function of the axial load in Figure 15. From Figure 14 it can be seen that for a sufficiently large imperfection amplitude, the first sharp maximum does

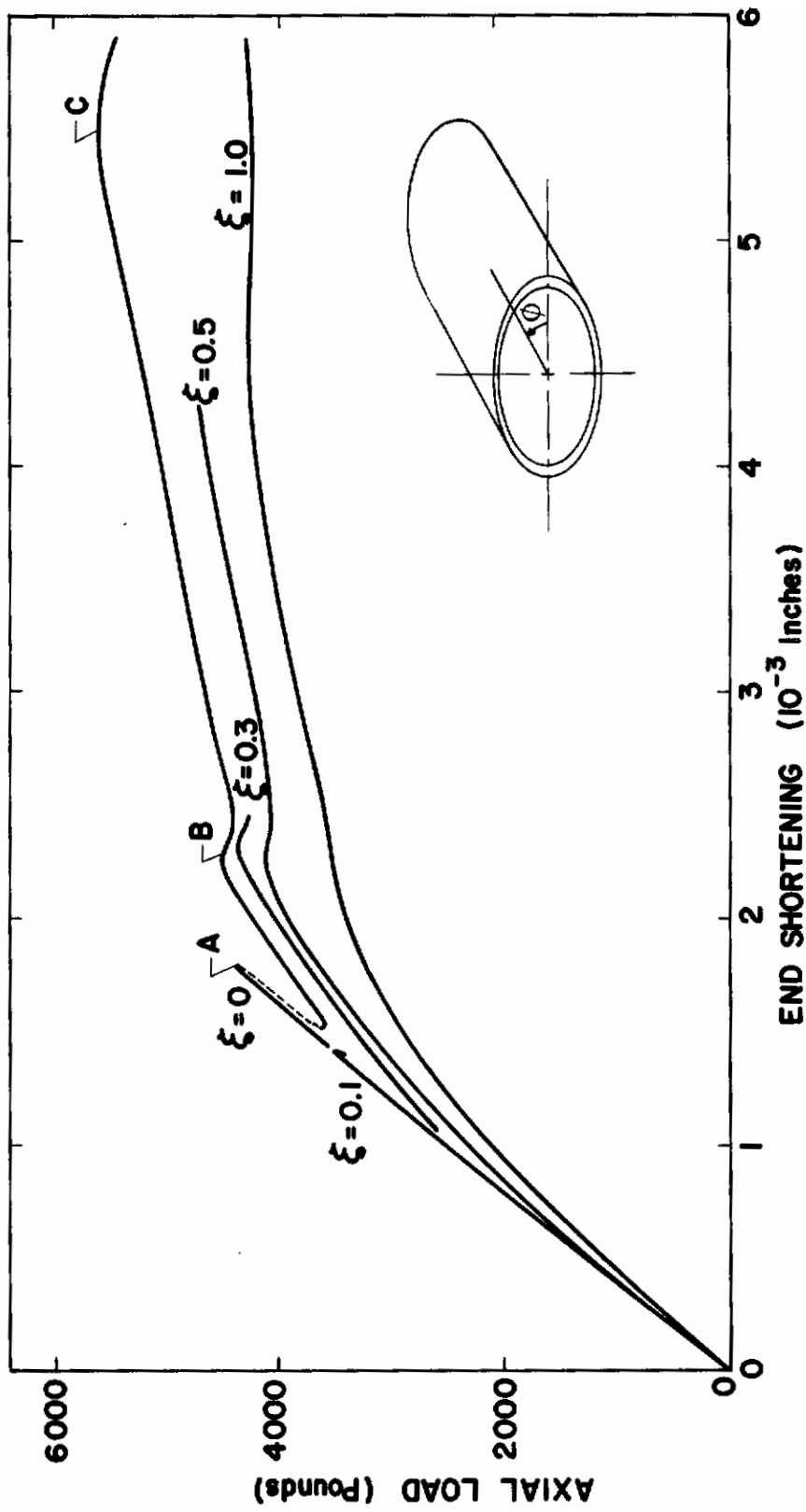


Figure 14 Load-Displacement Curves for Elliptic Cylinders

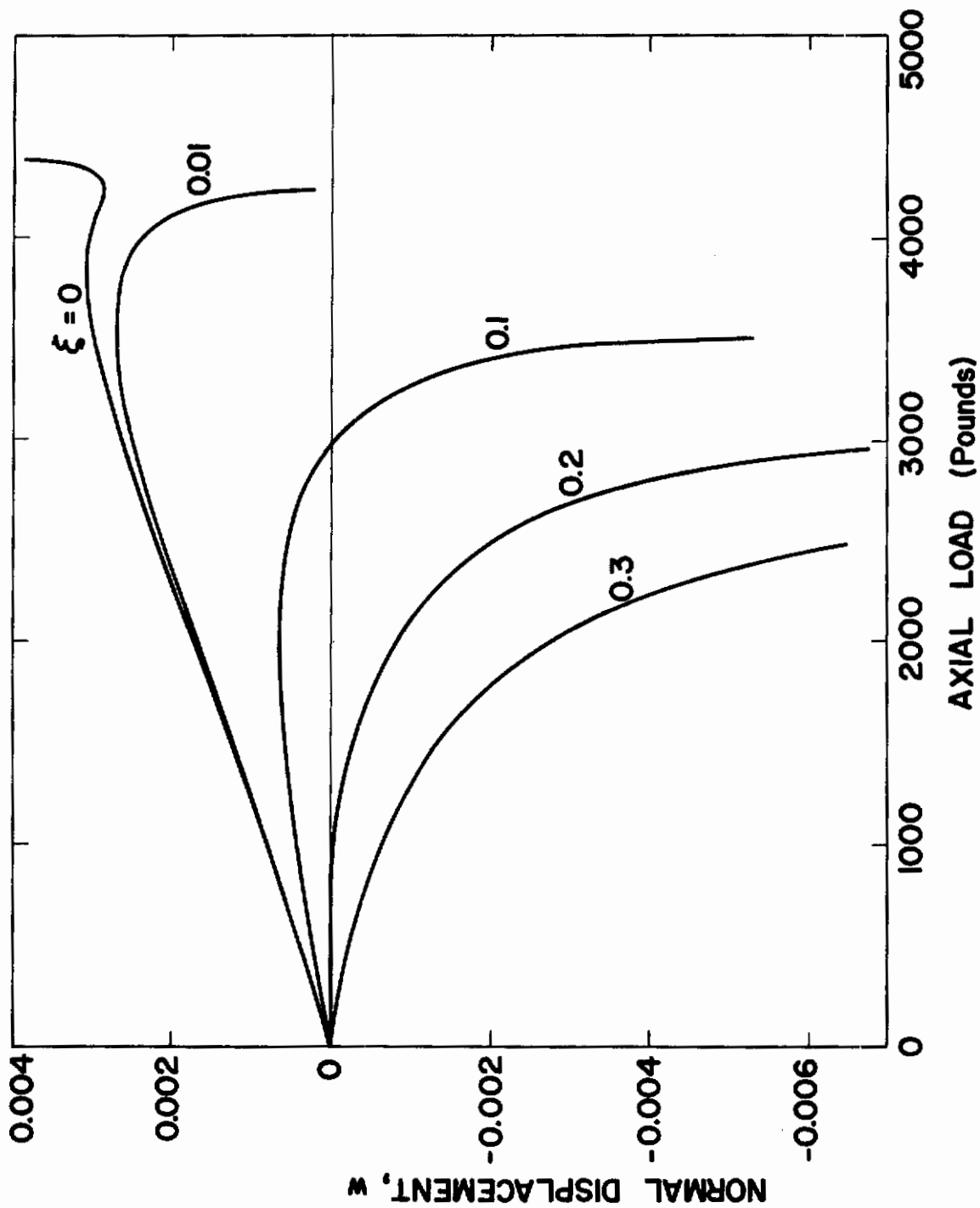


Figure 15 Normal Displacement Versus Axial Load

not exist--the curve is smooth and it is possible to find equilibrium configurations in the post-buckling range. After such configurations have been found, they can be used as starting values for an analysis in which the imperfection amplitude is gradually changed until a point is found on the post-buckling curve for perfect shells. After such a point is found, it is easy to establish post-buckling load displacement curves for perfect shells (Figure 14).

After the first sharp maximum the postbuckling curve exhibits two additional limit points which correspond to secondary buckling. The curve was not pursued beyond the third maximum because the deformations are then so large that the applicability of the basic equations is questionable. Also the buckle pattern is close to the point of maximum curvature and bifurcation into an antisymmetric mode is likely. The normal displacement as a function of the circumferential arclength at $x = L/2$ is shown in Figure 16. Curves are given for each of the three limit points (A, B, C on Fig. 14).

In the neighborhood of a limit point the developing collapse or buckle mode can be obtained as the difference between displacements for two neighboring solutions. Such collapse modes corresponding to each of the three points of maximum are shown in Figure 17. It can be seen that the point of maximum deflection in these patterns moves towards the point of maximum curvature as the end shortening increases. While the primary buckling load is rather sensitive to imperfections, it appears that the second maximum is not imperfection sensitive; hence, it may be suitable as a design limit. Results similar to these have been presented by Kempner, et al., for oval shells (Refs. 17, 18). However, Kempner's shells are not elliptic and a direct comparison is not possible.

A series of elliptic cones was also analyzed. Like the cylinders, the cones were loaded through uniform axial shortening. At the two ends rotation was unrestrained but the cross section was not allowed to deform. Four different cases (including a circular cone) were analyzed. The aspect ratio of the elliptic cross section was varied but the semi-axes of the ellipse were chosen such that the circumference was the same in all cases.

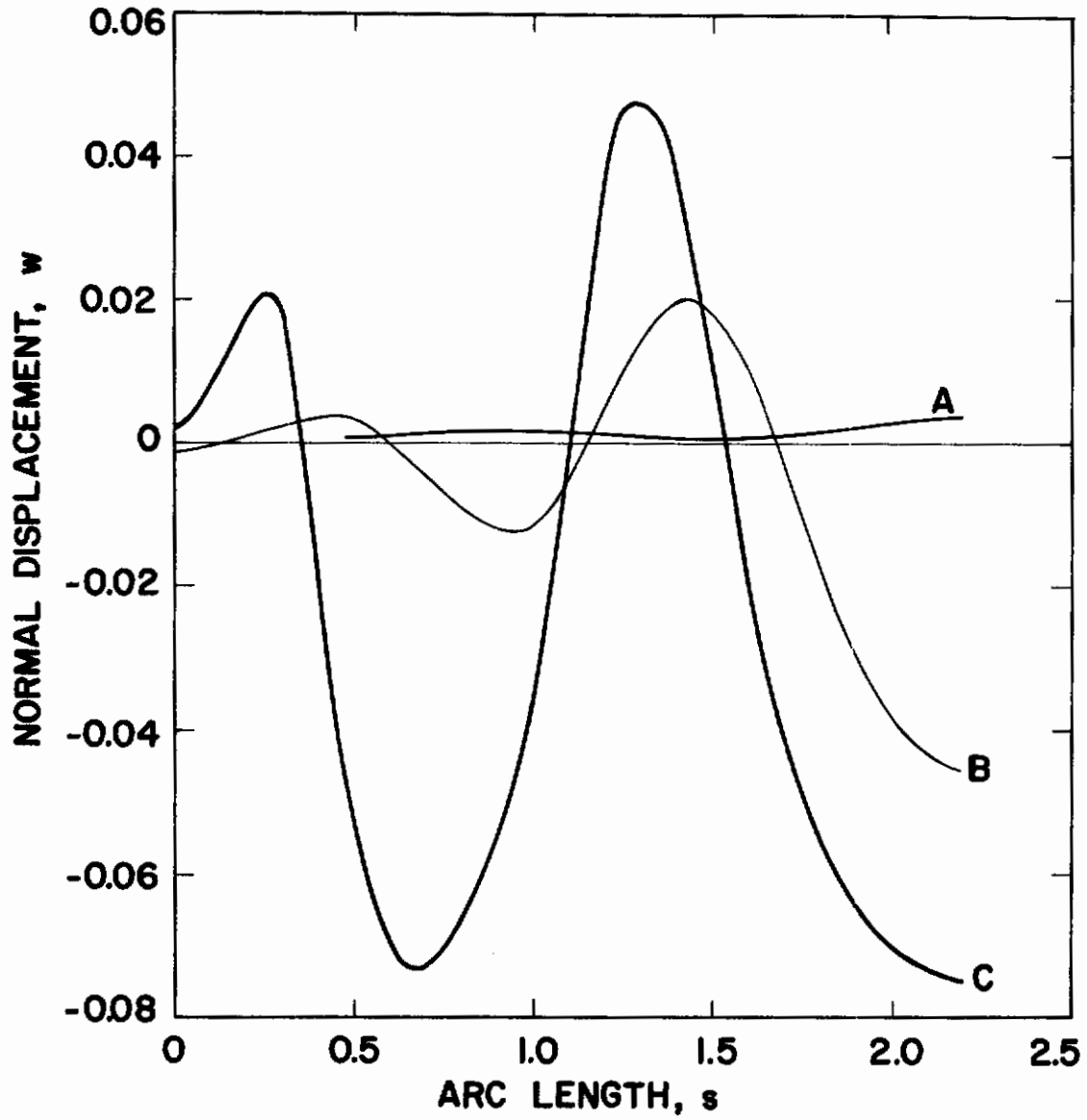


Figure 16 Normal Displacement Patterns at the Limit Points

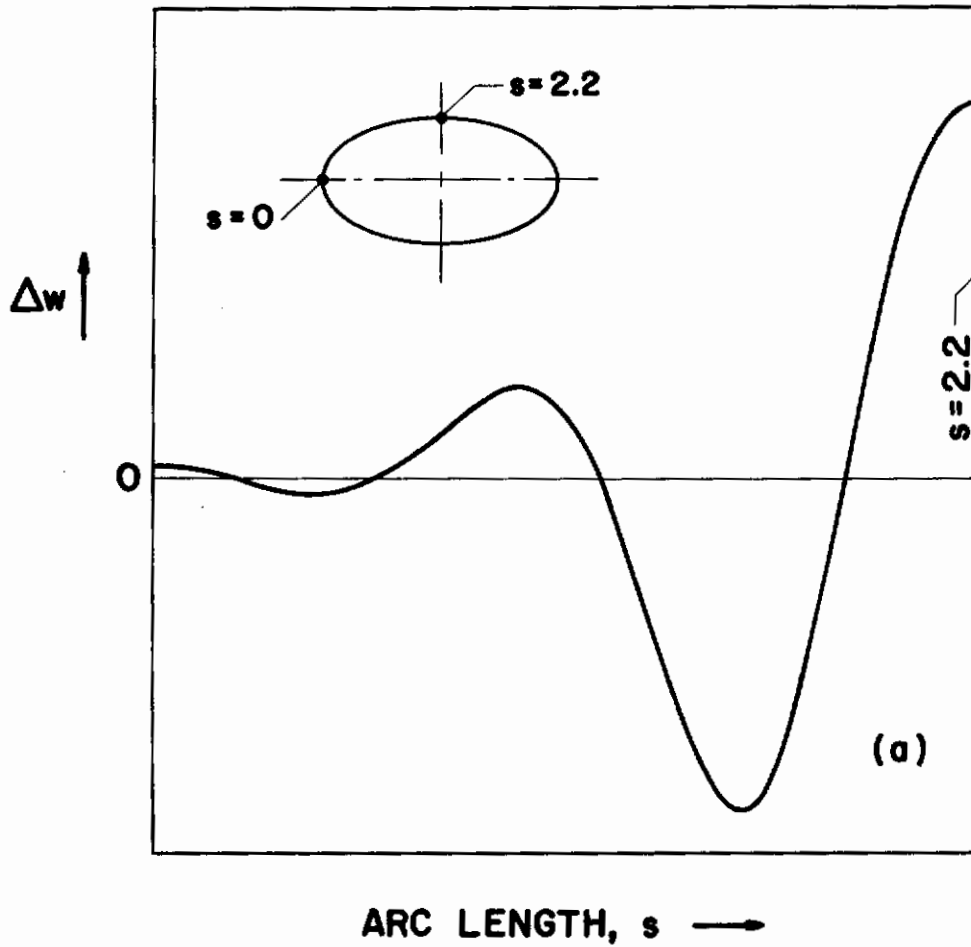


Figure 17(a) Buckling Patterns at Limit Points

Contrails

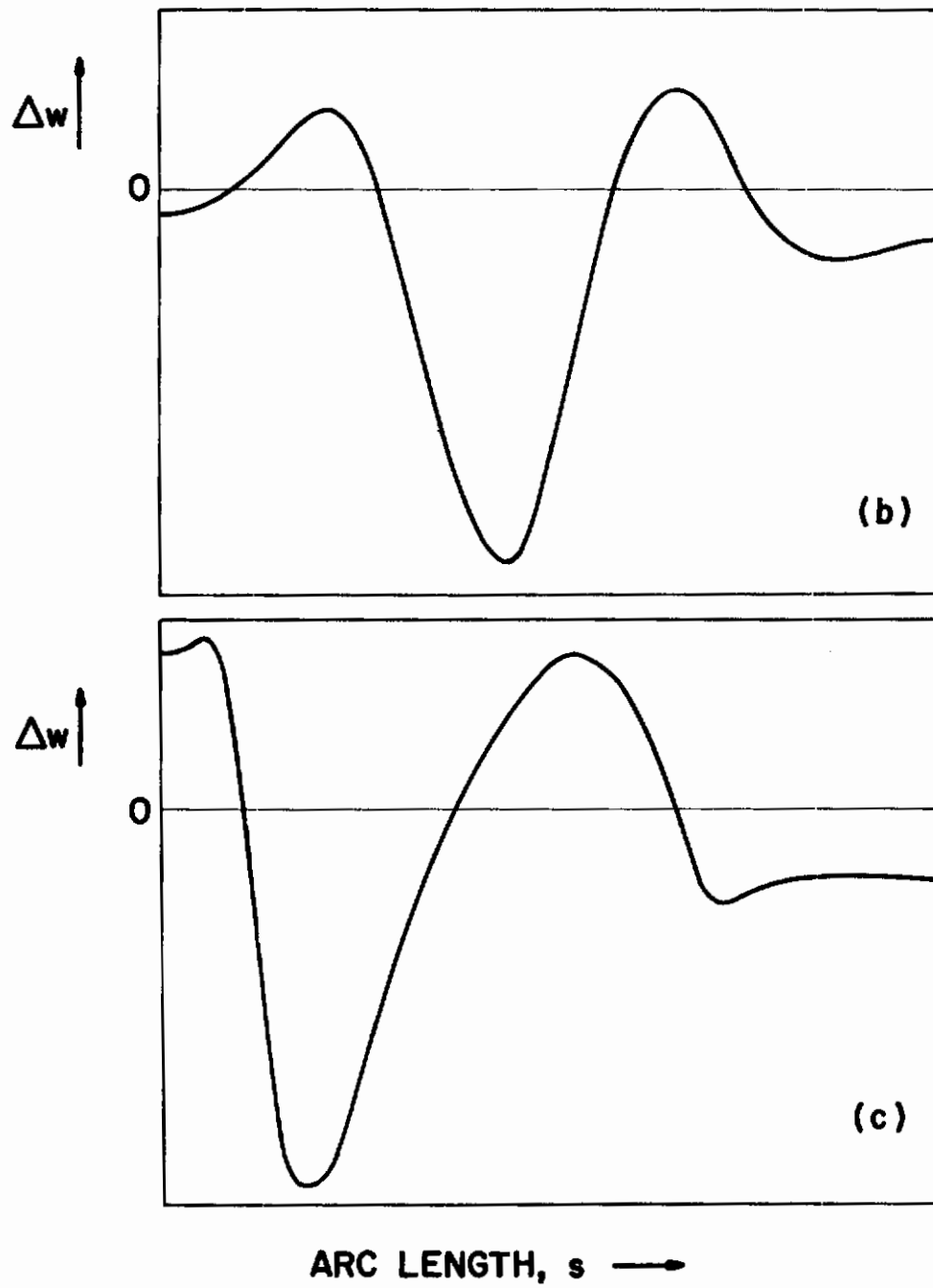


Figure 17 Buckling Patterns at Limit Points (Continued)

Young's modulus was chosen to be 10^7 psi and Poisson's ratio was 0.3. All the cones had the dimensions (see Fig. 18) $t = 0.16$ in., $c = 16$ in., and $d = 16$ in. The dimensions of the ellipse are shown in Table II.

Table II

Case	a (in.)	b (in.)
1	10.65	10.65
2	11.9	9.5
3	12.2	8.7
4	13.0	7.4

The results for the elliptic cylinders indicate that an imperfection with an amplitude of about one percent of the shell thickness will not significantly change the critical load. However, if this imperfection is included, a less severe convergence criterion may be used. Consequently, for economy in the analysis such an imperfection was included here. Figure 19 shows how the critical load varies with the ellipse ratio for elliptic cones of equal weight. The decrease in buckling load with increasing aspect ratio is less drastic than is indicated by the bifurcation buckling analysis for oval cylinders (Ref. 16). For the circular cone the bifurcation point and the maximum coincide but for higher values of the aspect ratio the critical load is above the bifurcation point. The buckling mode for Case 3 ($a/b = 1.4$) is shown in Figure 20. Similar results were obtained in a bifurcation buckling analysis for oval cylinders by Kempner, et al (Ref. 16).

It must be emphasized that for all the cases investigated here a uniform end shortening was applied to the shell. Had a uniformly distributed axial load been applied at both edges, the possibilities for redistribution of stresses would have been limited and the performance of the elliptic shells would have compared less favorably to shells with circular cross-section.

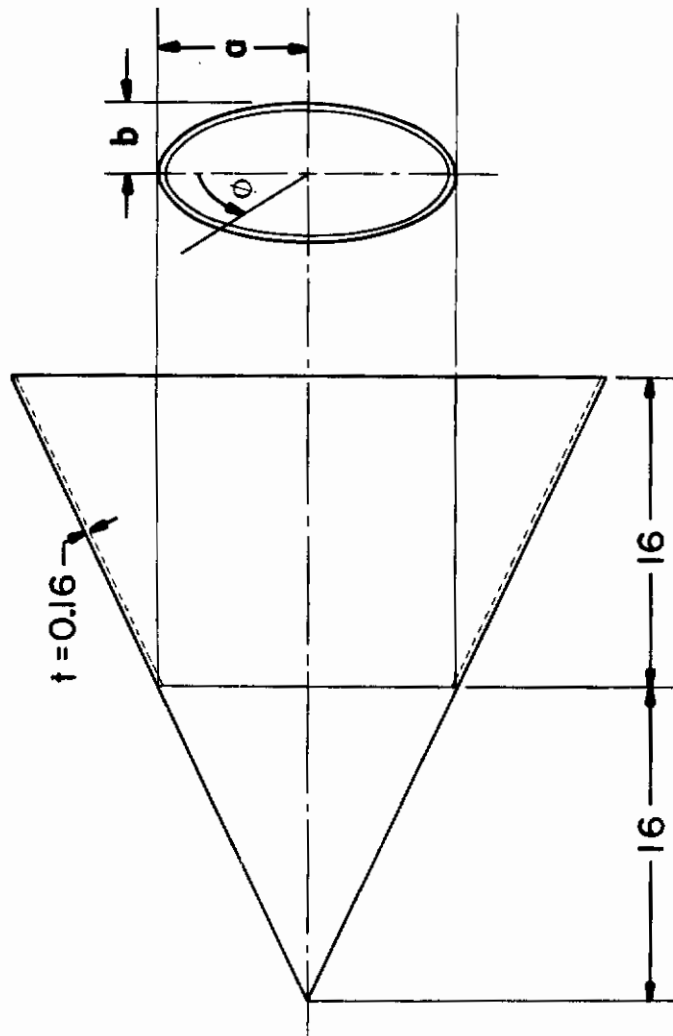


Figure 18 Elliptic Cone

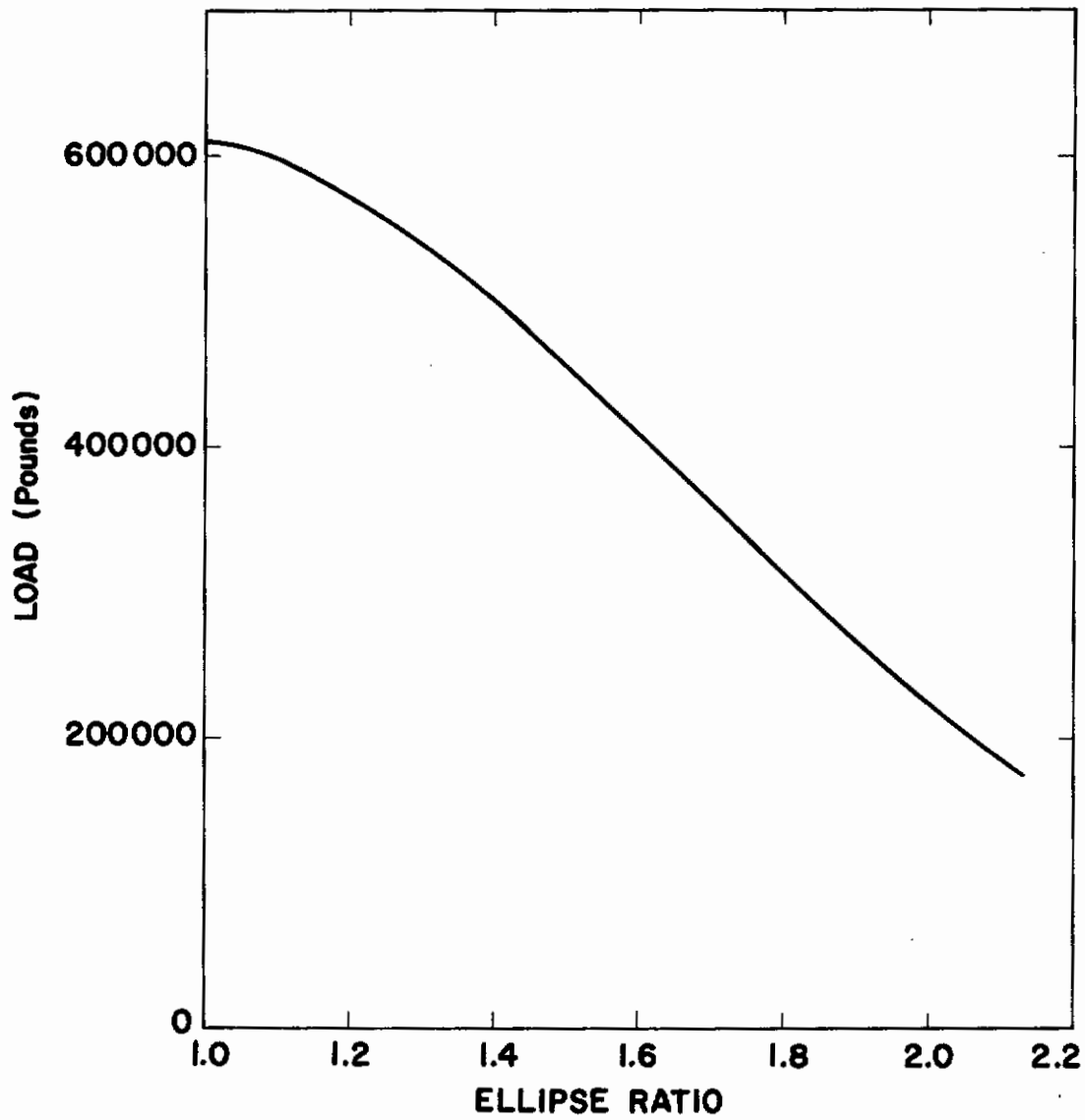


Figure 19 Ellipse Ratio

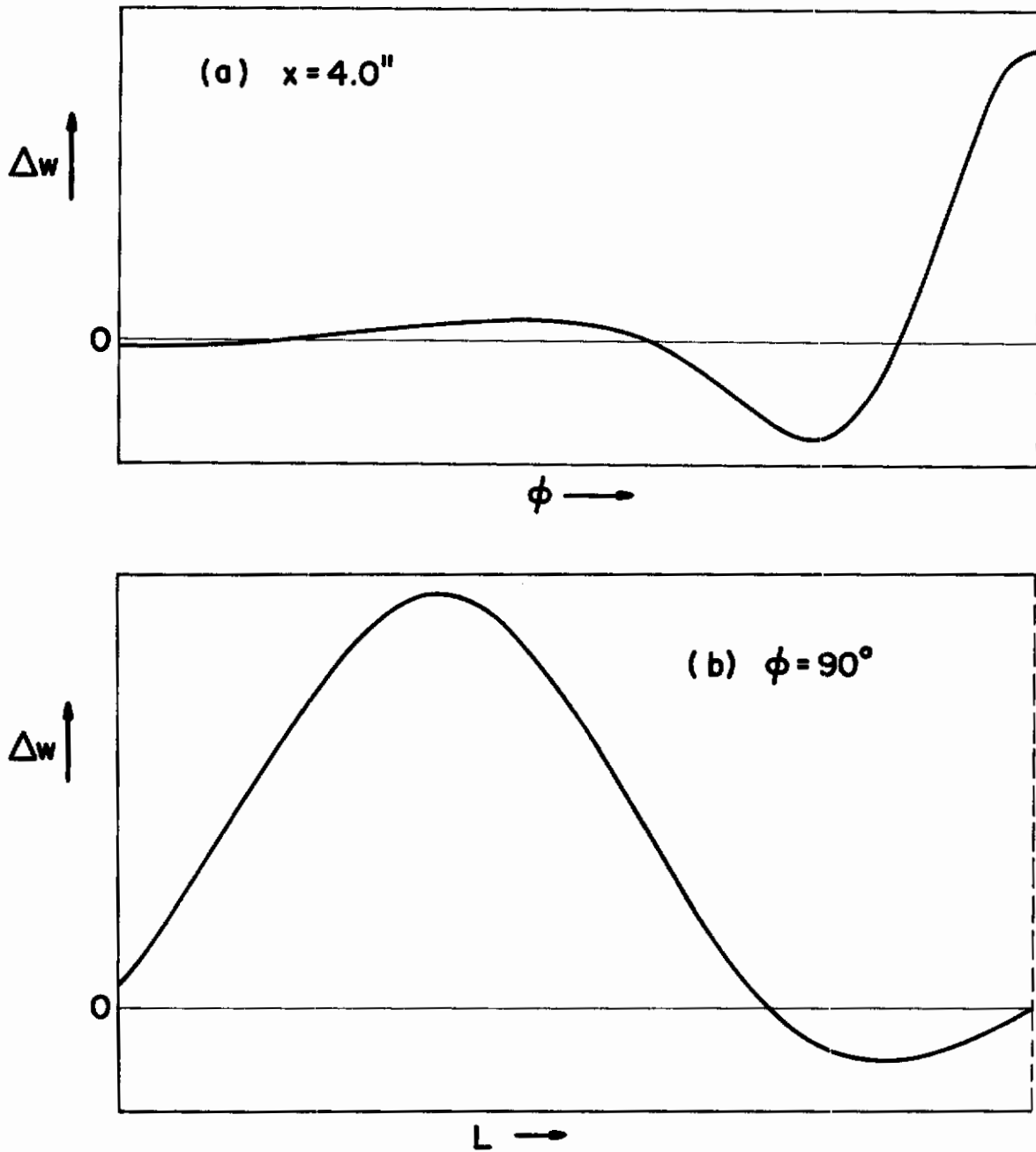


Figure 20 Buckling Patterns for Elliptic Cones

- a) at $x = L/2$
- b) at $\phi = \pi/2$

5.5 A Pear-Shaped Cylinder

In Figure 21 is shown a cylinder whose cross section consists of circular arcs joined by straight lines. The behavior of this shell subjected to uniform end shortening was investigated with use of the STAGS code.

As this type of shell is not included among the standard geometries, a subroutine must first be written for computation of the geometrical constants. The general procedure recommended in Reference 8 for computation of the geometrical coefficients can be greatly simplified in a case like this. If the arclength and the axial distance are chosen as surface coordinates, clearly the Lamé coefficients are $A = 1$, $B = 1$ and $C = 0$. Also the local radii of curvature are directly given.

As seen from Figure 22 the linear range in this case represents less than 1/30 of the total load history of the shell. The rapid change in slope of the load-deflection curves at about $P = 100$ lbs reflects the growth in normal deflection (buckling) of the flat portions of the shell. Associated with this growth in w is a redistribution of the axial stress so that the curved segments begin to take up a larger portion of the total axial load P . As more and more of the axial load is borne by the curved segments, the slope of the load-end-shortening curve increases until just before collapse, at which load the entire structure fails. Figures 23 and 24 show the circumferential distributions of normal outward displacement w and axial compression/length N_x at the shell midlength for $P = 2328$ lbs. At this load, both w and N_x are growing very rapidly with P in the curved portions $45^\circ \leq \theta \leq 90^\circ$ and $-67.5^\circ \leq \theta \leq 0^\circ$.

The rather complex behavior in this case indicates the need for a flexible strategy for calculation of collapse loads of shells. Small load steps and frequent refactoring of the equation system matrix are required in the load region between 100 and 200 lbs even though the displacements are relatively small in this range. Farther out on the load-end-shortening curve, where the displacements are larger, rather large load steps can be used and few refactorings are necessary. Efficient use of the STAGS code, or any code for predicting nonlinear behavior of shells, requires a sophisticated iteration strategy built into it and a well-trained user to take advantage

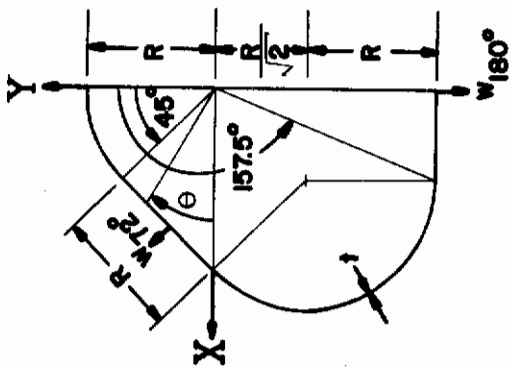


Figure 21 "Pear-Shaped" Cylinder Under Uniform End Shortening - Cylinder Geometry

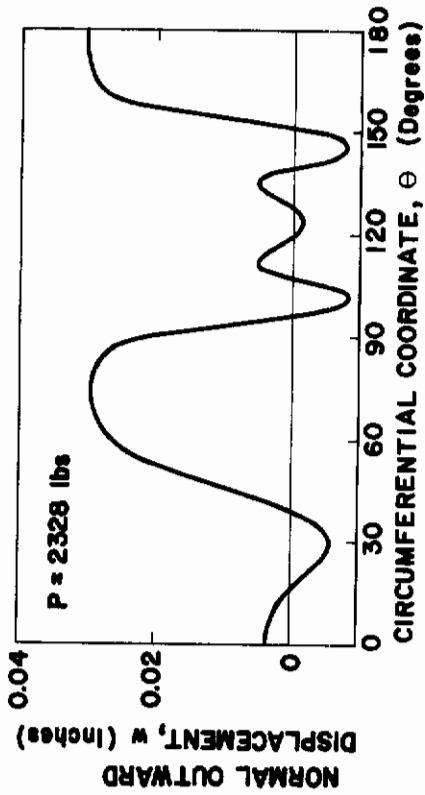


Figure 23 "Pear-Shaped" Cylinder Under Uniform End Shortening - Normal Displacement at Midlength at Collapse

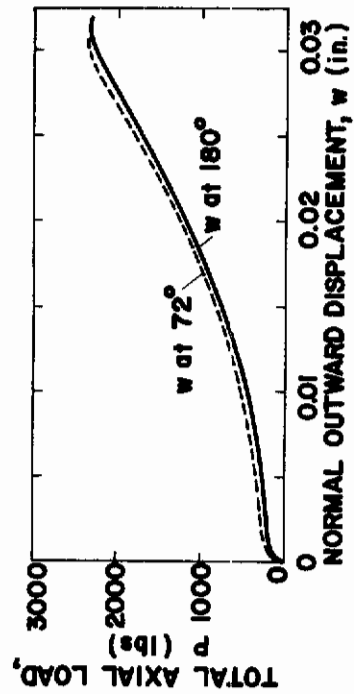


Figure 22 "Pear-Shaped" Cylinder Under Uniform End Shortening - Load-Deflection Curves

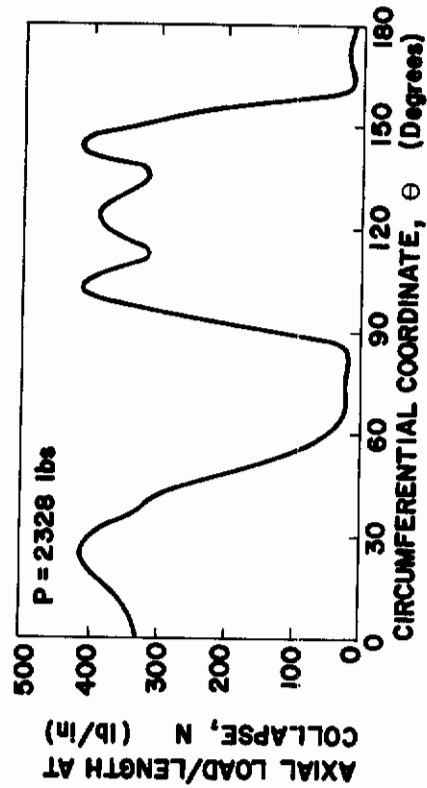


Figure 24 "Pear-Shaped" Cylinder Under Uniform End Shortening - Axial Line Load at Mid-length at Collapse

of this strategy.

A finite difference grid was used with 45 circumferential nodes and 9 axial nodes covering $1/2$ of the circumference and $1/2$ of the length. A variable spacing was used such that the gridlines would follow the intersections between flat and curved shell segments.

5.6 Bending of Cylindrical Panels Under Point Loading

The STAGS code was applied in an analysis of the behavior of shallow cylindrical panels as shown in Figure 25. The panels were subjected to bending through application of a point load at the midpoint of a panel supported at the curved edges and with the straight edges free. The behavior of such shells is expected to be highly nonlinear. If the load is applied towards the center of the circular arc, the cross-section will be more and more shallow with application of load and the result is similar to the well known Brazier effect. If the load is directed away from the center, the free edges will be under axial compression and the shell will collapse under a moderate load.

Three cases were considered: one with clamped edges loaded towards the center and two with simply supported edges; one loaded towards and one loaded away from the center. Ten axial and nine circumferential stations were used. The results, in terms of load displacement curves, are shown in Figure 26 for the shells with load toward the center, and in Figure 27 for the shell loaded away from the center. In the case with clamped edges, collapse is prevented by the development of axial membrane tension. Collapse in the case of simple support is indicated by a maximum in the load deflection curve. In a case like this, i. e., when the load is stepwise increased rather than a displacement, points on the curve cannot be computed through the maximum. At the point of maximum the equilibrium configuration is unstable and hence the coefficient matrix has a zero determinant. This determinant, as obtained when refactoring was required, is plotted versus the load in Figure 28. In this case, it is much easier to read the critical load from the determinant plot.

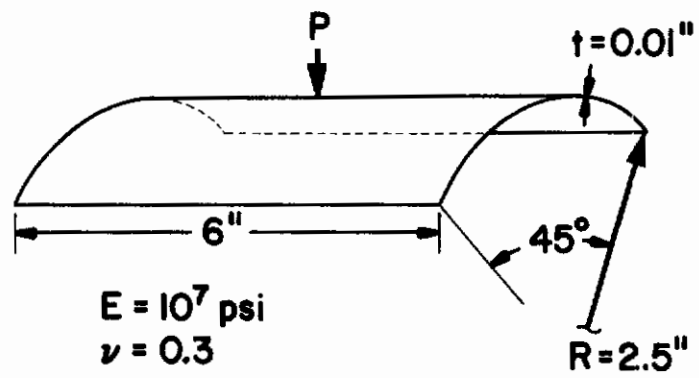


Figure 25 Cylindrical Panel With Point Load

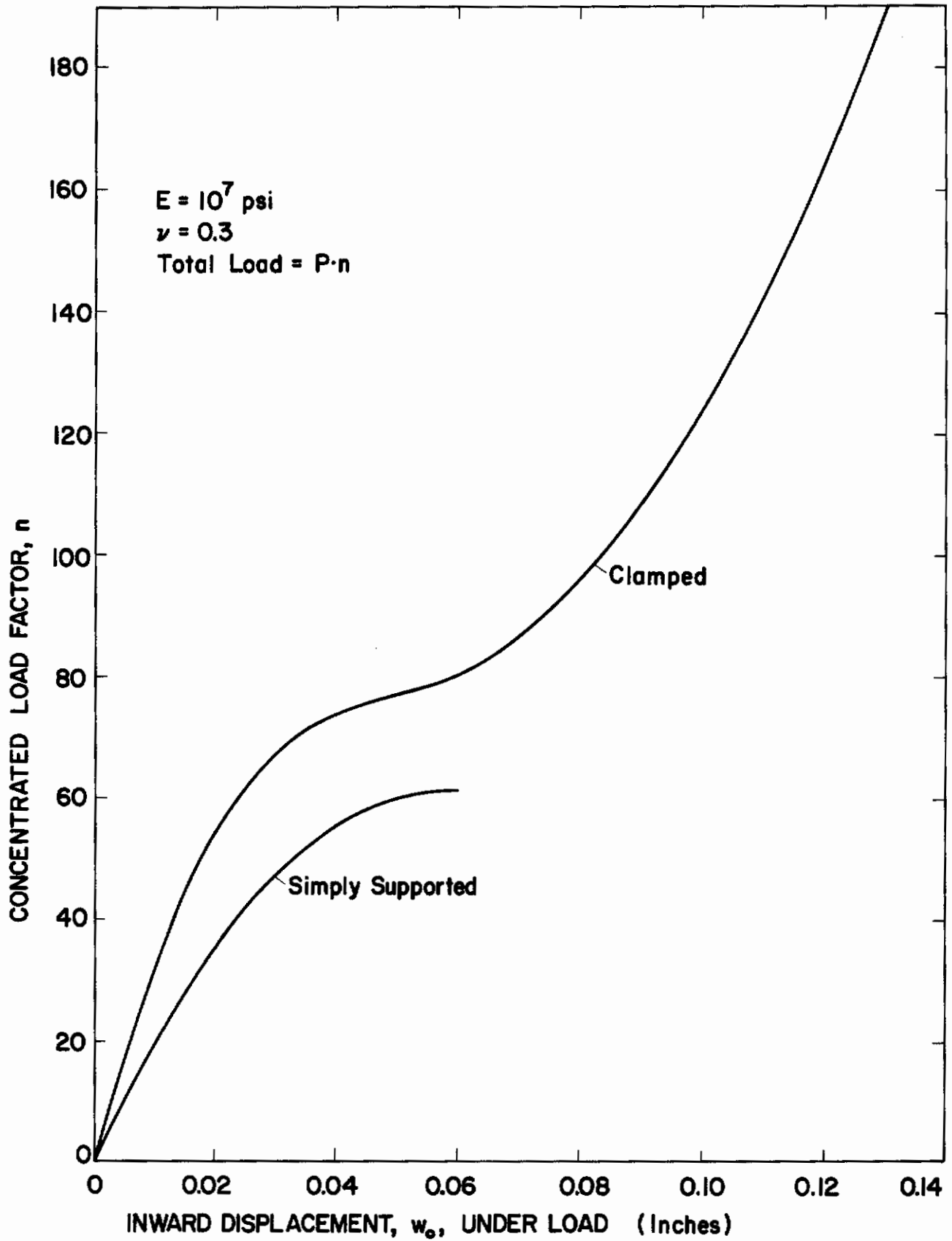


Figure 26 Load-Deflection Curves for Cylindrical Panels Loaded Towards the Center

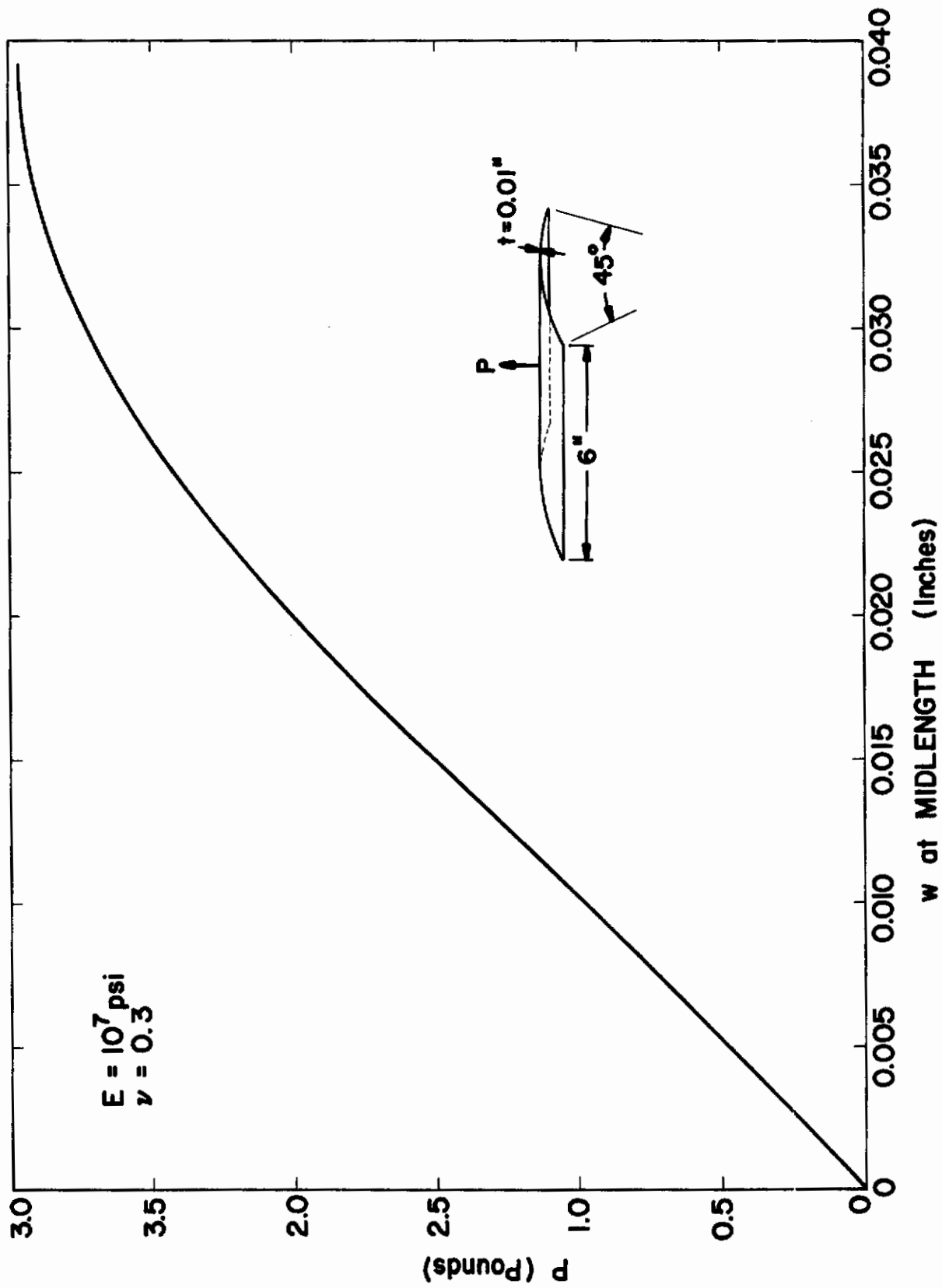


Figure 27 Load-Displacement Curve for Cylindrical Panel Loaded Away From Center

5.7 Inelastic Buckling of Plate

A flat plate was considered which was simply supported on two opposite edges and, on the other two edges, in-plane displacements were allowed but lateral displacements and rotation were suppressed. Axial compression was introduced in the plate at the simply supported edges. Plate dimensions and boundary conditions are shown in Figure 29.

In the elastic case the bifurcation buckling theory would be applicable and the value of the critical load can be obtained by use of simpler means than a nonlinear analysis. However, application of STAGS also gives information about the plate behavior in the post-buckling range. The critical load for the plate can be established by use of the nonlinear analysis if lateral displacements are triggered by small initial imperfections. As the lateral displacements grow very rapidly and if the imperfection amplitude is sufficiently small, the load-displacement curve has a sharp knee at the buckling load as it is traditionally defined. However, the smaller the imperfection is, the sharper must the convergence criterion be, and the more expensive is the analysis. For very small imperfections, it would be necessary to use double precision arithmetic. Therefore, advantage was taken of the fact that buckling is followed by redistribution of stresses. The curve corresponding to the difference between axial stress at the edge and axial stress at the center of the plate has a much sharper knee than the load displacement curve has and it is possible to determine the buckling load with larger values of the imperfections.

The method was demonstrated first for a plate which was assumed to remain elastic for any stress. A grid was used with 8 nodes along simply supported sides and 6 nodes along the clamped sides. The initial imperfection was given by

$$w_0 = 10^{-5} \sin \frac{\pi x}{L} \cos \frac{\pi y}{B}$$

The results for the elastic plate are shown in Figure 30. The plot of u versus σ indicates a value of a critical load of 2800 kg/cm^2 which is in close agreement with the result from the classical buckling analysis for plates.

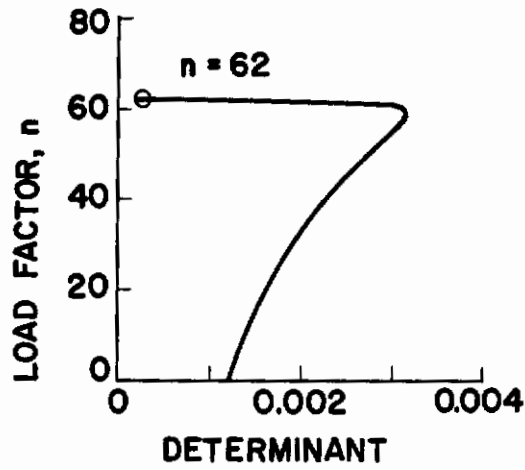


Figure 28 Determinant Versus Load Factor

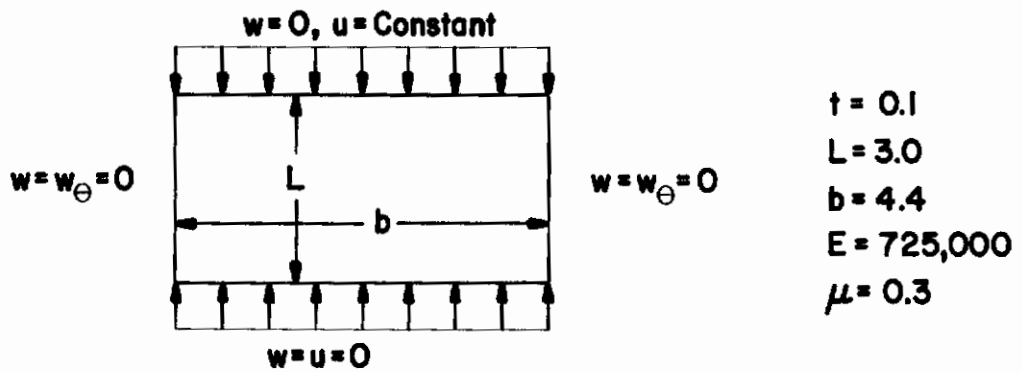


Figure 29 Plate in Compression

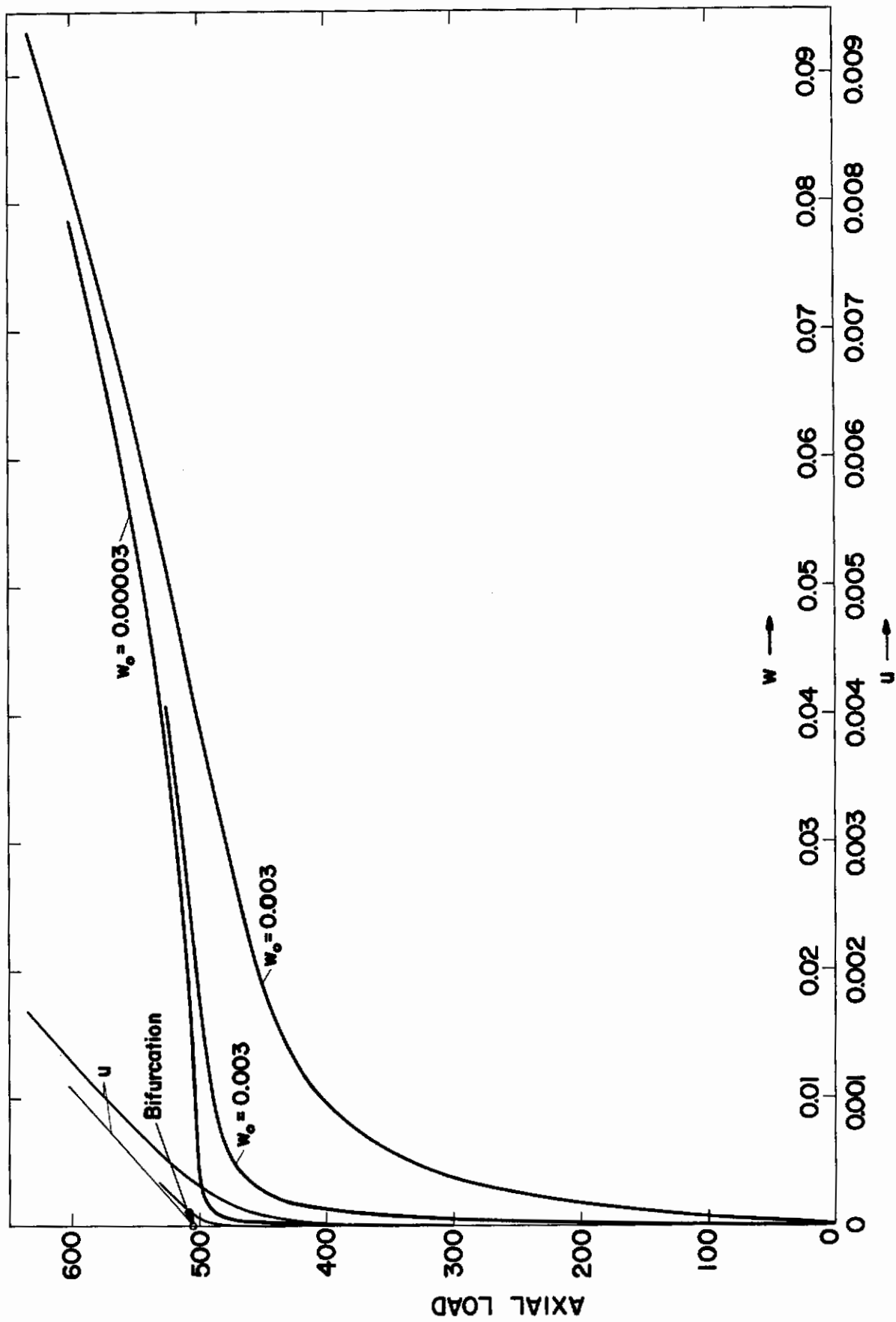


Figure 30 Load-Displacement Curves for Elastic Plate

The same analysis was also carried out for a 10 percent thicker plate, both elastic and inelastic with the stress-strain curve for uniaxial compression represented by the polygon shown in Figure 31. The results are shown in Figure 32 in the form of a load-displacement curve. A plot of the square of the displacement gives a clearer indication of the critical load. The critical stress is found to be 2270 kg/cm^2 corresponding to an axial load of 1100 kg. The kink in the curve for lateral displacement is presumably due to the fact that as the corner on the load displacement curve is reached by the average stress, the bending stiffness drops with the reduction in tangent modulus.

As the form of the load displacement curve above the second corner is in this case irrelevant, more accurate results would have been obtained if corner points had been concentrated in the neighborhood of the critical stress.

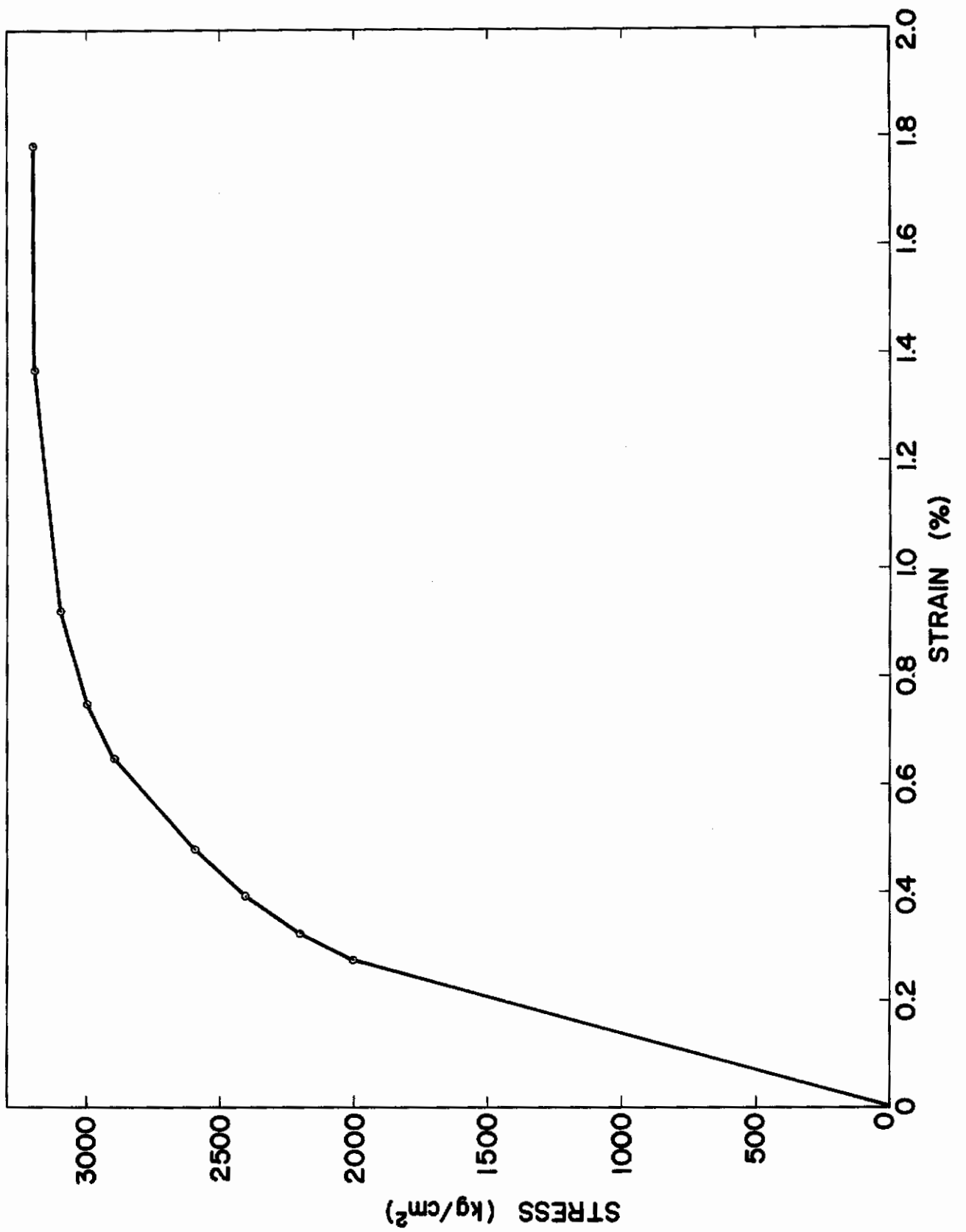


Figure 31 Stress-Strain Curve

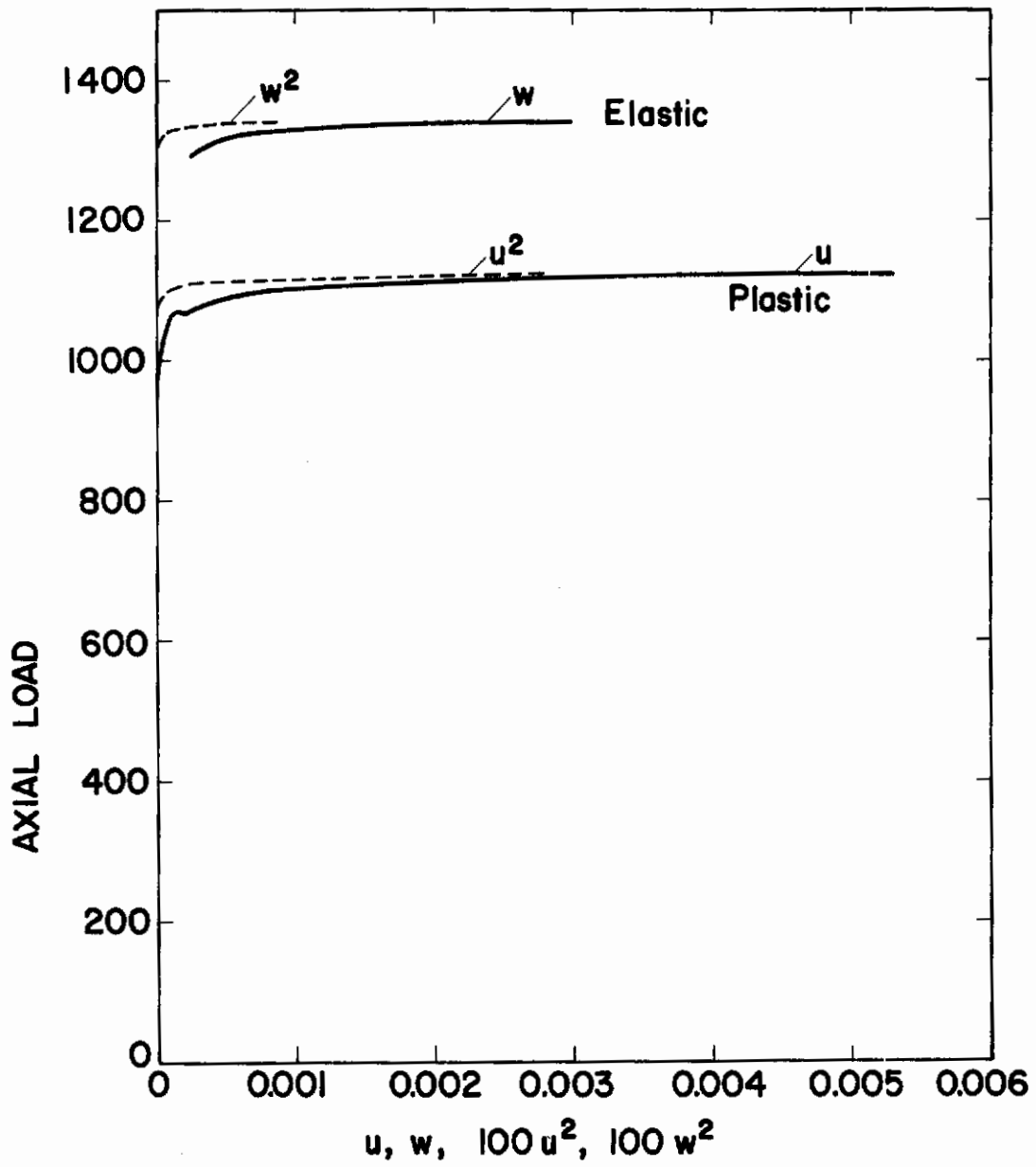


Figure 32 Load-Displacement Curves for Plate With $t = 0.11$ cm

Section 6.0

CONCLUSIONS AND RECOMMENDATIONS

Certain improvements or extensions of the STAGS computer program are reported here. It appears from solutions of several sample problems that with these extensions the STAGS computer program has become a powerful tool for the analysis of the nonlinear behavior of shells of general shape. The use of the energy method with finite differences appears to be attractive. For most shells, one of the standard geometry routines can be used, in which case determination of the input data generally is a matter of only a few minutes. Through comparison with other programs (Ref. 19), it has been found that the program is efficient with respect to computer time and to numerical stability. Likewise, the modified Newton-Raphson method appears to be the best choice for the solution of the nonlinear equation system. It has been favorably compared to other numerical methods in Reference 20. Finally, through application to a large number of practical cases, some with previously known solutions, the validity of the program has been reasonably well established in all its aspects. Under sponsorship of the NASA Manned Spacecraft Center in Houston, a series of tests of cylinders with cutouts has been carried out and results have been compared to analytical results from STAGS. The agreement between test results and analytical predictions is very good (Ref. 21).

In view of the successful application of the program, it appears desirable that further extensions be made. For instance, it would enhance the value of the program if the following items were included.

Improved input and output, particularly expanded plot capability including graphical display of the mesh generated by the program.

Contrails

Further improvement in program efficiency.

Input diagnostic.

Pre- and post-processors of data files.

Inclusion of some finite elements in the program such as bars and beams, which cannot be properly represented in the present program. Such a hybrid program would combine the efficiency of the finite difference analysis with the versatility of the finite element analysis.

Section 7.0

REFERENCES

1. R. F. Hartung, "An Assessment of Current Capability for Computer Analysis of Shell Structures," AFFDL TR-71-54, April 1971.
2. Lockheed Missiles & Space Company, Buckling Analysis of Segmental Orthotropic Cylinders Under Nonuniform Stress Distribution, by B. O. Almroth, F. A. Brogan, and E. V. Pittner, Sunnyvale, California, Report M-77-65-4, Vol. VIII, July 1965.
3. F. A. Brogan, B. O. Almroth, "Buckling of Cylinders With Cutouts," AIAA J., Vol. 8, No. 2, February 1970, pp. 236-241.
4. F. A. Brogan, K. Forsberg, and S. Smith, "Experimental and Analytical Investigation of the Dynamic Behavior of a Cylinder With a Cutout," AIAA Paper No. 68-318, AIAA/ASME 9th Structures, Structural Dynamics, and Materials Conference, April 1968.
5. Lockheed Missiles & Space Company, Analysis of Stiffened Shells With Cutouts, by F. A. Brogan and P. Stern, Report N-3M-69-1, Sunnyvale, California, 1969.
6. B. O. Almroth, F. A. Brogan, and M. B. Marlowe, "Collapse Analysis for Elliptic Cones," AIAA J., Vol. 9, No. 1, Jan. 1971, pp. 32-37.
7. B. O. Almroth and F. A. Brogan, "Buckling Analysis of General Shells," Lockheed Missiles & Space Company, LMSC D032008, December 1970.

8. B. O. Almroth, F. A. Brogan, F. Zele, User's Manual for STAGS, Final Report to Air Force Contract F33615-69-C-1523, AFFDL-TR-71-8, Vol. II.
9. M. B. Marlowe and W. Flügge, "Some New Developments in the Foundations of Shell Theory," LMSC 6-78-68-13, May 1968, Lockheed Missiles & Space Company, Palo Alto, California.
10. L. Collatz, Functional Analysis and Numerical Mathematics, Academic Press, New York, 1966.
11. D. Bushnell, "Analysis of Buckling and Vibration of Ring-Stiffened, Segmented Shells of Revolution," International J. Solids, Structures, Vol. 6, 1970, pp. 157-181.
12. S. Smith and B. O. Almroth, "An Experimental Investigation of Plastic Flow Under Biaxial Stress," Experimental Mechanics, June 1970, p. 217.
13. S. B. Batdorf and B. Budiansky, "A Mathematical Theory of Plasticity Based on the Concept of Slip," NACA TN 1371, 1949.
14. G. N. White, Jr., "Application of the Theory of Perfectly Plastic Solids to Stress Analysis of Strain Hardening Solids," Graduate Division of Applied Mathematics, Brown University, Providence, R. I., August 1950.
15. J. F. Besseling, "A Theory of Elastic, Plastic, and Creep Deformation of an Initially Isotropic Material," SUDAER Report No. 78, Department of Aero Engineering, Stanford University, 1958.
16. Lindberg, G. M., Olson, M. D., and Cowper, G. R., New Developments in the Finite Element Analysis of Shells, DME/NAE Quarterly Bulletin, No. 1969(4), January 1970.

17. J. Kempner and Y. -N Chen, "Buckling and Postbuckling of an Axially Compressed Oval Cylindrical Shell," Proceedings, Symposium on the Theory of Shells to Honor Lloyd Hamilton Donnell, University of Houston. McCutchan Publishing Corp., May 1967, pp. 141-183; also PIBAL Report No. 917, Polytechnic Institute of Brooklyn.
18. J. Kempner and Y-N. Chen, "Postbuckling of an Axially Compressed Oval Cylindrical Shell," Applied Mechanics, Proc. 12th Int. Congress Appl. Mech., Stanford University, August 26-31, 1968, pp. 246-268; also PIBAL Report No. 68-31, Polytechnic Institute of Brooklyn.
19. D. Bushnell and B. O. Almroth, "Finite Difference Energy Method for Nonlinear Shell Analysis," presented at the LMSC/AFFDL Conference on Computer Oriented Analysis of Shell Structures, Palo Alto, California, August 10-14, 1970.
20. B. O. Almroth and F. A. Brogan, "Practical Methods for Elastic Collapse Analysis for Shell Structures," presented at the AIAA/ASME 12th Structures, Structural Dynamics and Materials Conference, April 1971.
21. Almroth, B. O. and Holmes, A. M. C., "Shells With Cutouts, Experiment and Analysis," International Journal of Solids and Structures (to be published).

Contrails

Unclassified

Security Classification

DOCUMENT CONTROL DATA - R & D		
(Security classification of title, body of abstract and indexing annotation must be entered when the overall report is classified)		
1. ORIGINATING ACTIVITY (Corporate author) Lockheed Palo Alto Research Laboratory 3251 Hanover Street Palo Alto, California 94304	2a. REPORT SECURITY CLASSIFICATION <p style="text-align: center; font-size: large;">Unclassified</p> 2b. GROUP <p style="text-align: center;">N/a</p>	
3. REPORT TITLE <p style="text-align: center;">Collapse Analysis for Shells of General Shape; Volume I - Analysis</p>		
4. DESCRIPTIVE NOTES (Type of report and inclusive dates) Final Report April 1969-January 1972		
5. AUTHOR(S) (First name, middle initial, last name) B. O. Almroth F. A. Brogan M. B. Marlowe		
6. REPORT DATE August 1972	7a. TOTAL NO. OF PAGES <p style="text-align: center;">81</p>	7b. NO. OF REFS <p style="text-align: center;">21</p>
8a. CONTRACT OR GRANT NO. F33615-69-C-1523 b. PROJECT NO. 1467 c. Task No. 146703 d.	9a. ORIGINATOR'S REPORT NUMBER(S) <p style="text-align: center;">AFFDL TR-71-8, Vol. I</p> 9b. OTHER REPORT NO(S) (Any other numbers that may be assigned this report) <p style="text-align: center;">N/a</p>	
10. DISTRIBUTION STATEMENT <p style="text-align: center;">Approved for public release; distribution unlimited.</p>		
11. SUPPLEMENTARY NOTES None	12. SPONSORING MILITARY ACTIVITY Air Force Flight Dynamics Laboratory Air Force Systems Command Wright-Patterson Air Force Base, Ohio 45433	
13. ABSTRACT <p>This report presents a theory for nonlinear collapse analysis of shells with general shape. The theory combines energy principals and finite difference methods to obtain a system of nonlinear equations; these are solved by a modified Newton-Raphson technique. For greater economy and flexibility in the analysis a capability is provided for use of variable spacing finite difference grids. Inelastic material behavior, as predicted by the White-Besseling Theory, is incorporated into the analysis. A computer code, STAGS, based on the theory has been written and used to solve a number of sample problems. Results for these problems are presented.</p>		

DD FORM 1473
1 NOV 65

Unclassified

Security Classification

Security Classification

14. KEY WORDS	LINK A		LNK B		LINK C	
	ROLE	WT	ROLE	WT	ROLE	WT
1. Nonlinear Shell Analysis						
2. Finite Difference Methods						
3. Computer Analysis of Shells						
4. Plasticity						
5. Collapse of Shells						
6. Bifurcation Buckling of Shells						
7. Energy Methods						
8. Shell Analysis						
9. Structural Analysis						